Sensitivity of the IceCube Enhancements to Cosmic Ray Air Showers

Empfindlichkeit der IceCube-Erweiterungen gegenüber Luftschauern der kosmischen Strahlung

Bachelor's Thesis of

Antonia Elisa Jaumann

At the KIT Department of Physics
Institute of Experimental Particle Physics (ETP)

First examiner:	Prof. Dr. Ralph Engel
Second examiner:	Dr. Andreas Haungs
Advisor:	Dr. Fahim Varsi

08. May 2025 – 10. November 2025

Karlsruher Institut für Technologie
Fakultät für Physik
76128 Karlsruhe

Sensitivity of the IceCube Enhancements to Cosmic Ray Air Showers (Bachelor's Thesis)

I declare that I have developed and written the enclosed thesis completely by myself. I have not used any other than the aids that I have mentioned. I have marked all parts of the thesis that I have included from referenced literature, either in their original wording or paraphrasing their contents. I have followed the by-laws to implement scientific integrity at KIT.

Karlsruhe, 10. November 2025

. . . .
(Antonia Elisa Jaumann)

For the purpose of improving the English language and the overall readability, DeepL and ChatGPT were employed. Furthermore, ChatGPT was selectively used to refine the presentation of some plots.

Abstract

Sensitivity of the IceCube Enhancements to Cosmic Ray Air Showers

The surface detector IceTop of the IceCube Neutrino Observatory is being extended, among others, with scintillators. In addition, the in-ice components are being expanded within the framework of the planned IceCube Upgrade, which includes the deployment of seven new strings at reduced spacing. Both enhancements provide improved opportunities for the measurement of cosmic rays and their secondary particles.

Simulation studies offer the possibility of systematically evaluating the benefits of such new detector concepts in advance. By generating and analyzing simulated data, detector responses can be modeled and investigated with respect to specific questions. Such a simulation study is the subject of this thesis.

For three exemplary scintillator stations, the trigger efficiency for the detection of cosmic-ray-generated air showers was determined. Furthermore, for the same stations an event reconstruction was performed, from which both the core position resolution and the angular resolution were derived.

Another focus of this work lies in the investigation of high-energy muon responses within the volume of the Upgrade. In this way, prospects are made about the number of air shower cores that can be detected by the IceCube Upgrade.

Zusammenfassung

Empfindlichkeit der IceCube-Erweiterungen gegenüber Luftschauern der kosmischen Strahlung

Der Oberflächendetektor IceTop des IceCube-Neutrino-Observatoriums wird unter anderem durch Szintillatoren erweitert. Auch die In-Ice-Komponenten erfahren im Rahmen des geplanten IceCube Upgrades eine Erweiterung, die den Einbau von sieben neuen Strings mit geringeren Abständen umfasst. Beide Ausbaumaßnahmen eröffnen verbesserte Möglichkeiten zur kosmischer Strahlung und deren Sekundärteilchen.
Simulationsstudien bieten die Möglichkeit, derartige neue Detektorkonzepte bereits im Vorfeld systematisch zu evaluieren. Durch die Erzeugung und Analyse simulierter Daten lassen sich Detektorantworten modellieren und hinsichtlich spezifischer Fragestellungen untersuchen. Eine entsprechende Simulationsstudie ist Inhalt und Gegenstand der vorliegenden Thesis.
Exemplarisch für drei Szintillator-Stationen wurde die Trigger-Effizienz bestimmt, mit der kosmische Luftschauer detektiert werden können. Darüber hinaus erfolgte für dieselben Stationen eine Ereignisrekonstruktion, aus der die Auflösung von sowohl des Ankunftsortes, als auch des Winkels der Schauerachse abgeleitet wurden.
Ein weiterer Schwerpunkt der Arbeit liegt auf der Untersuchung der Detektorantworten hochenergetischer Myonen im Volumen des Upgrades. Auf diese Weise lassen sich Aussagen über die Anzahl der durch das IceCube Upgrade erfassbaren Schauer treffen.

Contents

1

Introduction

Cosmic Rays (CRs) are high-energy particles from space. They reach energies of up to 10^{20} eV [1] and can travel large distances through the universe. They originate from processes that are still unexplored, such as galactic supernova remnants or extragalactic origins [2]. After being accelerated in such environments, they can undergo a wide variety of processes like interaction with matter surrounding the source, diffusion in interstellar magnetic fields or spallation. Some particles also make it to Earth. When they encounter the atmosphere, large quantities of secondary particles are created within a cascade. Investigations of these particle avalanches can make it possible to reconstruct the original particle. This in turn is important for obtaining more information about the source of the high-energy CR.

However, detection is associated with many difficulties. Since detection of high-energy particles can only take place indirectly via the cascades, the secondary particles of a so-called Extensive Air Shower (EAS) must be detected. They undergo complex interactions and in addition, fluctuations occur between individual showers of the same primary mass and energy. Reconstructing the properties of the original particle is also complicated. In addition, particle flux decreases dramatically at high particle energies [3]. In order to perform a statistically reliable detection, extremely large detectors with different detector types must be used. One such detector is the IceCube Neutrino Observatory (ICNO) at the South Pole.

The ICNO is dedicated to the detection of high-energy neutrinos [4]. The two-part design, however, allows for the investigation of neutrino events in the in-ice detector as well as the detection of secondary particles from CRs [5] in the IceTop (IT) detector. Various types of detectors have already been installed. In addition, an upgrade to IceCube-Gen2 is currently in plan, which will expand the existing experiment with a larger number of detectors of different detector types. The upgrades are intended to improve the precision of the measurements and thus increase the sensitivity to the energy and mass composition of CRs.
Two important components of the expansion are the surface enhancement, which is equipped with scintillators and radio antennas, and the pre-performed IceCube Upgrade, which consists of seven new strings and reaches a depth of about 2500 m [6]. While the IceCube Upgrade was primarily developed for precision measurements of neutrino oscillations [4], it also opens up new possibilities for the investigation of high-energy muons from CRs.

Considering the imminent installation in the austral summer of 2025/26, a precise analysis of the expected performance and scientific potential of the upgrades is particularly important. Since real measurement data will only be available after deployment, simulation studies offer a crucial opportunity to evaluate the detector performance in advance. In such studies, events are first generated that describe the interactions of CRs in the atmosphere. The response of the planned detectors to these particles is then to be modeled. This enables a comprehensive analysis of relevant issues, which at the same time provides reliable predictions and identifies starting points for optimization.

For example, simulated data enables a comparison between the properties of the original particle and the reconstructed particle based on the detector responses and reconstruction. Since the true position and direction of the particle is known, the potential of the detector can be evaluated by determining the differences to the reconstructed particle. This aspect is also part of this work. With the help of a multi-step analysis of simulated data, it is possible to investigate, e.g., how well the shower geometry can be reconstructed using the algorithms based on, for example, three new scintillator stations. Furthermore, it is possible to investigate the efficiency of the scintillation detectors for detecting air showers.

Another interesting question concerns how many showers can be detected by the seven new in-ice strings of the Upgrade. The muon information from simulations is used for this purpose.

All these aspects and questions are combined in this thesis with the aim of evaluating the potential of the scintillators and the Upgrade, or more precisely, quantifying the sensitivity of the Upgrade to CR air shower cores.

To achieve this, this work is structured as follows. After a brief introduction to general CR physics, a description of the IceCube experiment follows. Both the aims of the experiment and the individual components are discussed. This is followed by a detailed analysis of the above-mentioned aspects. This can be divided into two parts. The first part deals with the analysis related to the scintillator stations, which focuses on the simulation data from a total of three stations, starting with the efficiency of these stations. This is followed by an analysis of the reconstruction by the same three stations, with focus on angular and core resolution. At the end of the first part of the analysis, the resolutions are compared with the resolution of a single station.

The second part contains the analysis related to the IceCube Upgrade. Here, muon propagation is performed, which shows how many showers reach the Upgrade. The results are first presented for the entire simulation dataset. In order to establish a connection to the scintillator stations discussed in the first part, the results are finally also presented in this context.

2 Cosmic Ray Physics

In the beginning of the 20th century, the physicist Victor F. Hess was investigating a pervasive radiation whose cause could be not explained at that time. He carried out a total of seven balloon flights and took measurements at an altitude of a few thousand meters until he was able to say with certainty that this pervasive radiation couldn't have its origin on Earth. It is coming from outside and then hit the atmosphere, where it causes ionization. In addition, there are strange fluctuations in intensity on Earth and an increase with altitude. He repeated the measurements at night and during a solar eclipse and found that there are similar results. By this, he conducted that the radiation is not exclusively coming from the Sun.

What Hess had investigated in 1912 was considered cosmic radiation at the time, i.e. radiation that originated in the galaxy [7]. Nowadays, these radiations are referred to as Cosmic Rays (CRs).

2.1 Introduction to Cosmic Rays

CRs are energetic particles traveling through space. Most of these particles are protons, but they can also be heavier particles like fully ionized iron nuclei or other heavy nuclei. Their energies cover a range from several hundred MeV up to hundreds of EeV, thus from 10^8 to at least 10^{20} eV [1].

The investigation of the energy spectrum helps to understand the astrophysical phenomenon responsible for the acceleration and propagation of CRs. Therefore, the spectrum is plotted as a function of energy in Figure 2.1. On the y-axis is the differential flux, i.e. the number of particles per unit area, unit time, solid angle and energy interval. The CR energy spectrum follows a steeply falling power law of a spectral index of about 2.7 and in Figure 2.1 it is multiplied by $E^{2.6}$ so that the most important features become better visible. There is a steepening between 10^{15} and 10^{16} eV that is called *knee*. A steepening indicates that the flux of CRs falls more rapidly with their energy. There is a second steepening at around 10^{17} eV, the *second knee*. So far, there are only theories and no complete explanation for the steepening in the slope. The third feature depicted in Figure 2.1 is the *ankle* at around $10^{18.5}$ eV, where the slope becomes flatter again. A better understanding of the slope changes can be correlated with a much better understanding of the propagation and origin of CRs.
In order to give the study of CRs some structure in terms of designations, the energy spectrum is divided into three areas. The low-energy region contains the range up to 100 TeV, the high-energy region from 100 TeV to 1 EeV and the ultra-high-energy region contains energies above 1 EeV [2]. The low-energy region is partly of solar origin and is often influenced by solar modulation due to the strong magnetic field. Considering CRs with energies between 1 PeV and 1 EeV, there is a transition between galactic origin, such as accelerated at supernova remnants, and extragalactic origin. CRs with an energy above 1 EeV, thus ultra-high-energy CRs, are assumed to have an extragalactic origin [1].

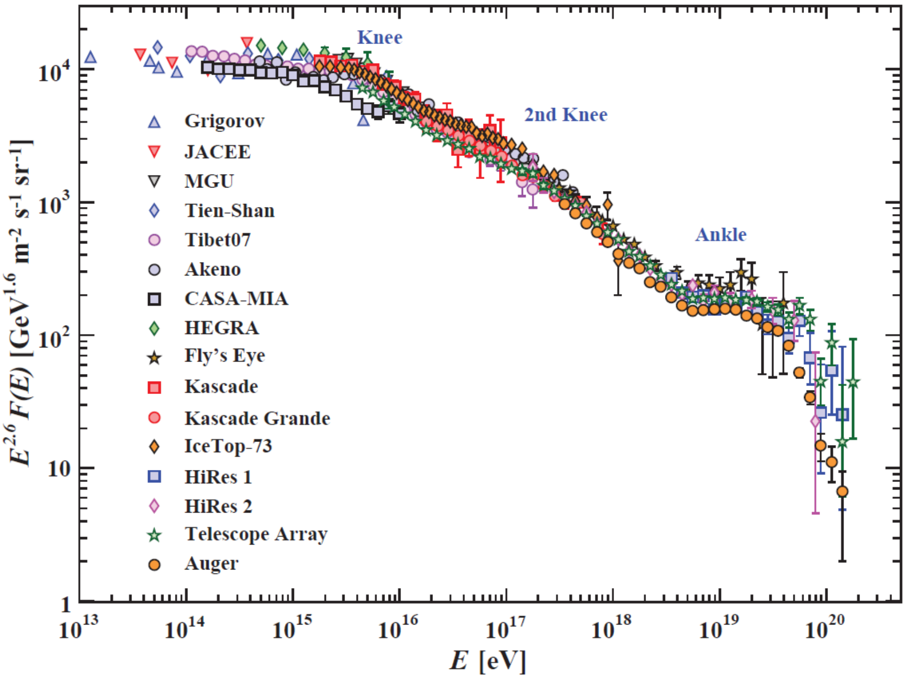

Figure 2.1.: Energy spectrum of CRs. The differential flux F(E) is shown as a function of energy from different experiments. The plot is taken from [3].

What is observed at the surface on Earth usually is not a primary CR. After traveling through space, the CRs interact with the atmosphere. This interaction creates many secondary particles in a cascade that is called an EAS. It is precisely these secondary particles that are observed and measured on Earth. The next sections therefore focus on EASs and their detection.

2.2 Extensive Air Showers

The main properties of EASs are depicted in Figure 2.2 on the left. The starting point of an EAS is at the atmospheric depth at which a primary particle of the CR interacts with molecules of the atmosphere for the first time. It is called the first interaction point. This is where a cascade of secondary particles starts. It mainly propagates along the so called shower axis, which follows the direction of the primary particle. The point where the shower axis reaches the ground is called shower core. The secondary particles spread laterally around the shower axis and therefore do not arrive collectively at the shower core, neither in time nor in position. A shower front is therefore formed. It has a higher density around the shower axis and is curved as depicted in the figure. The shower plane is the plane perpendicular to the shower axis. Due to the curved structure of the shower front, a delay in the arrival times of the particles in comparison to the shower plane occurs. This delay and the thickness of the shower disk is used to describe the shower front.

The right side of Figure 2.2 shows an atmospheric cascade with its different components. The different components arise after the interaction of the primary CR particle with a nucleus in the atmosphere. These hadronic interactions produce neutral and charged pions, as well as other nucleons, which is forming the hadronic backbone of the shower, also called the hadronic component. Neutral pions usually decay in to two photons and start the electromagnetic branch. The charged pions lead to muons, which form the muonic component. The charged pions also generate neutrinos, which are called the atmospheric neutrinos [8].

It can therefore be stated that the electromagnetic and hadronic showers are the two main components of an EAS. The type of shower is defined by the primary. While electromagnetic particles produce electromagnetic showers, the CR-nuclei produce hadronic showers. Muons are an indicator for hadronic showers, since electromagnetic showers have nearly zero muons. Both components can be described by simplified models. The Heitler model is used for the electromagnetic component, which was extended by Matthews for the hadronic component [9].

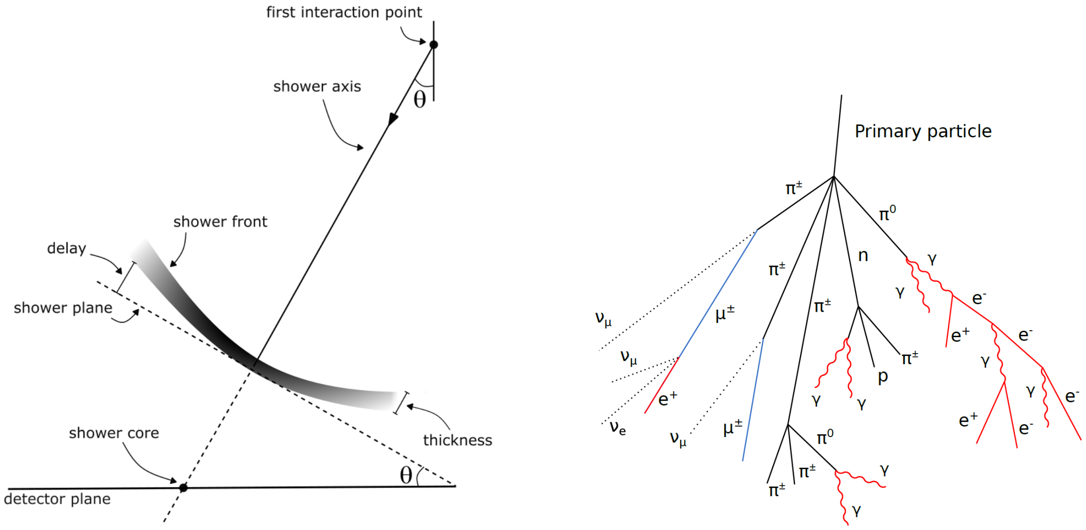

(a) **(b)**

Figure 2.2.: Scheme of an EAS with its main properties (a) and the generation of a cascade with different components (b). (a): The shower starts at the first interaction point and it expands along the axis. The shower plane is perpendicular to the shower axis, but the particles build a so called shower disk that is curved and has a higher particle density near the core. (b): A primary particle generates an electromagnetic (red), a muonic (blue), a neutrino (dotted) and a hadronic (black) component of the cascade. (a) is inspired and (b) taken from [2].

2.2.1 Electromagnetic Showers

As already mentioned, showers are starting right after an interaction of a primary particle with the atmosphere and they consist of many thousand up to millions of secondary particles. This leads to the conclusion that there are a large number of processes that take place during the formation and propagation of an air shower. This means that it is very complex and not easy to describe such an air shower in detail. Simplified assumptions therefore had to be made to enable a physical description that includes the most important properties of air showers. This was done for electromagnetic showers by Walter Heitler [9].
The assumptions made and the resulting physical relationships can be explained with the

help of Figure 2.3. The shower begins with a photon and the first split happens at n=1. n is the number of splitting lengths d. It is defined as

$$d = \lambda_r \ln 2, \tag{2.1}$$

where λ_r represents the radiation length. Here, the first assumption becomes apparent: The energy of the original particle splits symmetrically between the two resulting components. This in turn means that after n splitting lengths, there are 2^n particles. The second assumption is also immediately apparent. The figure only shows electrons/positrons (e^-/e^+) and photons (γ). It is assumed here that there are no other energy losses apart from bremsstrahlung and pair production, which leads to the diagram shown. The repeating pattern is therefore as follows: The incoming photon undergoes pair production and produces an e^-/e^+-pair. Each of those particles then undergoes bremsstrahlung, which includes the production of one photon. Each subsequent e^-/e^+ produces bremsstrahlung and each γ created produces an e^-/e^+-pair and so on. Another assumption is that these processes continue until a critical energy E_c^e is reached. The corresponding number of splitting lengths is n_c.

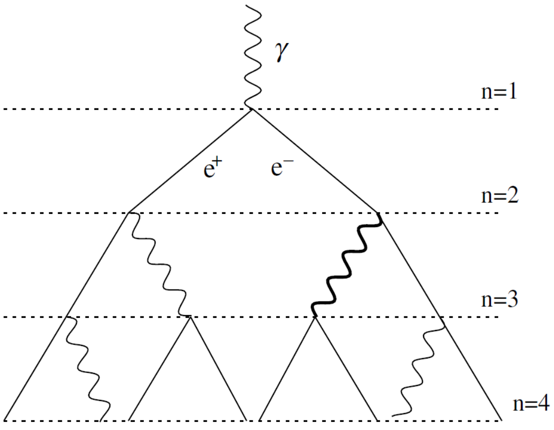

Figure 2.3: Electromagnetic cascade using the Heitler model. It shows the starting point (top) of an electromagnetic cascade and how the shower develops. Taken from [9].

The most important relationships from the Heitler model are the relationship between the shower maximum N_{max}, i.e. the position of the shower development where the number of particles reaches its maximum before the shower dies out, and the initial energy of the primary particle E_0, as well as the relationship between E_0 and the depth of the shower maximum X^{γ}_{max}. They are

$$E_0 = E_c^e N_{max} \tag{2.2}$$

and

$$X^{\gamma}_{max} = n_c \lambda_r \ln 2 = \lambda_r \ln \frac{E_0}{E_c^e}. \tag{2.3}$$

In the case of electromagnetic showers, E_c^e is the energy, at which collisional energy loss is more likely than radiative energy loss. Equations 2.2 and 2.3 show some interesting and fundamental relationships in the description of electromagnetic showers. On the one hand, the maximum number of particles, also called the shower maximum, is directly proportional to the energy of the primary. High-energy primaries are therefore expected to produce more secondary particles than low-energy primaries. On the other hand, the depth of this shower maximum is proportional to the logarithm of the initial energy. Hence, the more energy the primary particle has, the deeper in the atmosphere the shower maximum is located, albeit with a logarithmic proportionality [9].

2.2.2 Hadronic Showers

The mathematical description of hadronic showers is more complex. It was expanded by John Matthews in 2005 [9]. However, before physical relationships are explicitly mentioned, the principle of hadronic showers should be explained first.

Hadronic air showers are initiated by a primary particle, which is usually a proton or, in most cases, a heavier nucleus. It reacts with the atoms in the atmosphere and the resulting particles consist of about 80% pions [10]. Those pions can be charged ($\pi^{\pm}$) or neutral (π^0) and they in turn decay through the following processes:

$$\begin{aligned} \pi^0 &\longrightarrow \gamma + \gamma \\ \pi^+ &\longrightarrow \mu^+ + \nu_\mu \\ \pi^- &\longrightarrow \mu^- + \bar{\nu}_\mu \end{aligned} \tag{2.4}$$

While the neutral pions form an electromagnetic branch that follows the laws mentioned in section 2.2.1, the charged pions either continue to interact or decay according to the decay process mentioned above in equation 2.4.

Similar to electromagnetic showers, there is the assumption of symmetrical energy distribution and symmetrical splitting into $\pi^{\pm}$ or π^0. Thus the number of particles splits after a splitting length into N_{ch} charged pions and $N_{ch}/2$ neutral pions. The energy is divided into $2/3$ for the charged pions and $1/3$ for the neutral pions, so after n layers. the $(N_{ch})^n$ charged pions have the energy

$$E_{\pi^{\pm}} = \left(\frac{2}{3}\right)^n E_0. \tag{2.5}$$

Respectively for a single charged pion

$$E_\pi = \frac{E_0}{(\frac{3}{2}N_{ch})^n}. \tag{2.6}$$

However, the splitting length d' is defined by the interaction length λ_I with

$$d' = \lambda_I \ln 2. \tag{2.7}$$

Also similar to electromagnetic showers, there is a critical energy E_c^π at which the hadronic shower ends. E_c^π is defined as the point at which the distance to the next interaction point becomes greater than the decay length of $\pi^{\pm}$. This leads to the decay into muons ($\mu^{\pm}$). Since one $\pi^{\pm}$ decays into one $\mu^{\pm}$, it can be stated that $N_\mu = N_\pi$.

The number of $\mu^{\pm}$ and $e^{\pm}$ produced depends on both the primary energy and the type of the incoming cosmic ray. For a proton with the atomic number A=1, the following dependencies apply

$$N_\mu^p = \left(\frac{E_0}{E_c^\pi}\right)^\beta \tag{2.8}$$

$$N_e \sim E_0^\alpha. \tag{2.9}$$

Since $\alpha = 1.03 > 1$ and $\beta = 0.85 < 1$, both the number of electrons and muons increases with increasing primary energy, but with different rates.
Looking at other primary particles than proton, the relationship

$$N_\mu^A = N_\mu^p A^{0.15} \tag{2.10}$$

applies, where the atomic number of the primary particle must be used for A. In conclusion, it can be said that nuclear showers have more muons than proton showers.
The same procedure can also be used for the depth of the shower maximum X_{max}^A, so that ultimately the relationships

$$X_{max}^p = X_{max}^\gamma + X_0 - \lambda_r \ln(3N_{ch}) \tag{2.11}$$

and

$$X_{max}^A = X_{max}^p - \lambda_r \ln A \tag{2.12}$$

are found. X_0 is defined as the first interaction point at $X_0 = \lambda_I \ln 2$. Thus, the shower maximum for nuclear showers is set higher in the atmosphere as for proton-showers [9].

Above all, the last mentioned aspects, which indicate the connection between the properties of a shower and the type of the primary, play an important role in this thesis. In the following aspects of this work, the behavior of different primaries are compared several times. Only with keeping those physical correlations in mind, the emerging observations can be interpreted correctly.

2.3 Detection Methods

There are two options for detecting CRs: direct or indirect detection. Direct detection can only take place at an altitude of a several tens of kilometers, preferably completely above the atmosphere, so that there is no interaction with the atoms in the atmosphere. Examples of this would be balloons or satellites, which can directly determine the mass and energy of the CRs. However, there are a few limitations to direct detection. Firstly, the size and weight of the detector are severely limited due to their installation above the atmosphere. Secondly, the differential flux decreases with increasing energy, as can be seen in Figure 2.1, so that ultimately only CRs with an energy up to 10^{14} or 10^{15} eV can be detected [8].

Therefore, another method of detection was developed. This is the indirect measurement, which takes place on the Earth's surface. So it is a method that detects the EASs. The detectors must be able to register the passage of a particle and measure its deposited energy [8]. This is followed by a multi-step reconstruction of the primary particle.
The indirect detection method often uses entire arrays of individual detectors. A possible arrangement is a hexagonal geometry, as can also be found in the IceCube experiment. The advantage of this geometry is that the relative distances between the individual detectors are always the same. In addition, such an arrangement can be scaled as often as required [8]. This depends on the size of the EAS, i.e. the primary energy that is to be detected.
Just as important as a clever arrangement is a trigger for the detectors. A trigger is a setting that determines when a detector starts to detect. This means that certain conditions are created in advance, and the measurement starts when these are met. Common conditions

are a minimum energy deposit of the secondary particles or a certain time window in which several signals must be measured. This ensures that only meaningful events (in the sense of the targeted primary energy range) are measured and then analyzed.

There are different types of detectors for EASs that utilize different properties. Particles, Cherenkov radiation, emission of radio waves or fluorescence light emitted by the particles of the EAS during the shower development in the atmosphere are frequently used. The IceCube experiment is based on Cherenkov detectors to measure the secondary particles of the shower. As this work is embedded in the IceCube experiment, this type of detection is examined in more detail in the following.

The basis of Cherenkov detectors is the generation of so-called Cherenkov light when particles pass through a medium at a velocity greater than the phase velocity of light in this medium. This causes a brief polarization of the medium. Due to the resulting electric dipole moment, electromagnetic waves are emitted. The individual electromagnetic waves interfere constructively to form a wavefront, which becomes visible as a so-called Cherenkov cone.

The opening angle θ of the Cherenkov cone results in

$$\cos\theta = \frac{1}{\beta n}, \tag{2.13}$$

where n is the refractive index of the medium and $\beta = \frac{v}{c}$ is the speed of the particle divided by the speed of light [11].

The Cherenkov photons produced can now be measured in suitable detectors. As an example, in air under standard conditions, a particle produces roughly 10–20 Cherenkov photons per meter traveled. For relativistic particles with $\beta = 1$, the number of photons emitted per unit length is proportional to $1 - \frac{1}{n^2}$ [12]. Consequently, in a denser medium, like ice or water, where the refractive index n is higher, the number of photons increases by roughly a factor of 700 compared to air. With many particles present, a detector therefore needs to measure both the large number of photons and their arrival time [8]. A large number of Cherenkov detectors are used at IceCube. There are Cherenkov tanks on the surface as well as an entire in-ice detector that uses ice as a medium. The so-called Digital Optical Modules (DOMs) can detect the Cherenkov light, but more on this in chapter 3.2.

3 The IceCube Neutrino Observatory

The IceCube Neutrino Observatory (ICNO) is an observatory dedicated to the study of high-energy astrophysical neutrinos. It is located in Antarctica near the Amundsen-Scott South Pole Station [4] and uses one cubic kilometer of Antarctic ice as a detector [13]. This makes the ICNO currently the world's largest neutrino detector. This large size is necessary because neutrinos have an extremely low probability of interaction with matter. For example, although about 10^{14} neutrinos fly through a human body every second, due to the extremely low interaction probability of neutrinos, one would still have to wait 100 years until an interaction of the neutrino within the body can actually be measured [4].

Consisting of the surface detector IT and an in-ice detector IceCube, the IceCube experiment extends to a depth of about 2500 meters. In 1990, Antarctic Muon and Neutrino Detector Array (AMANDA) demonstrated that the Antarctic ice is well suited for investigating and detecting energetic neutrinos. Based on these findings, IceCube was set up at the South Pole within 6 years and was completed in December 2010 [4]. For a better understanding of the individual components of the IceCube experiment, which will be discussed in the following section 3.2, the scientific objective and the actual intentions of IceCube will now be discussed in a few words.

3.1 Aims of the IceCube Experiment

Particles from astrophysical sources in space have to travel a long way and overcome many obstacles before they reach the Earth. If the particles are electrically charged, interstellar magnetic fields cause them to deviate from their original path. This makes it difficult to accurately determine the direction of the source of the particle [14]. In contrast, the electrically neutral gamma rays and neutrinos are not deflected by the magnetic field and since neutrinos, as already mentioned at the beginning of this chapter, hardly interact with any matter, they are ideal for probing farther and deeper to astrophysical sources, which is a central objective of the IceCube experiment.

ICNO detects neutrinos from all directions, including those penetrating through the Earth. The primary background for astrophysical neutrinos, especially those coming from above, comes from the interaction of CRs with nuclei while traveling through the atmosphere, generating atmospheric muons and neutrinos [15] that also reach the detector. In order to distinguish the astrophysical neutrinos from atmospheric signals, IceCube relies on its specific detector design and event selection strategies. Hence, the two detector parts focus on neutrino detection (in-ice) and CR detection (IT). This is why the components of the IceCube experiment are chosen as described in the following sections.

3.2 IceCube

Both parts of the IceCube observatory, the surface detector IT (measuring air showers) and the in-ice component IceCube (the actual neutrino telescope), are depicted in Figure 3.1.

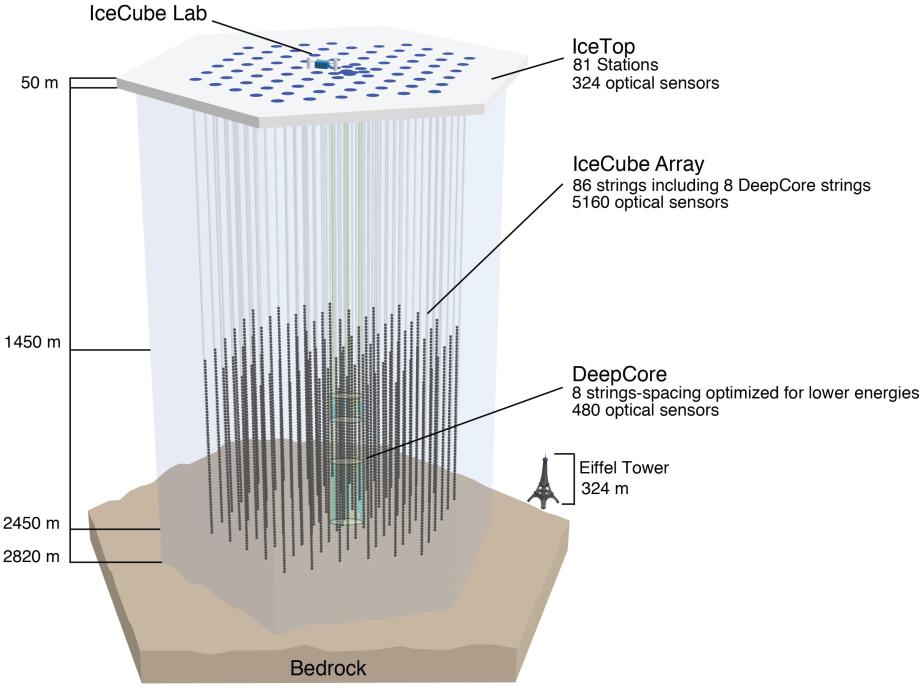

Figure 3.1.: Schematic of the IceCube Neutrino Observatory ICNO. The illustration shows the main components: surface detector IT, IceCube in-ice array, DeepCore and the position of the IceCube Laboratory. Credit: IceCube Collaboration [4].

Directly on the surface is the IceCube laboratory, where all data is first collected before it can be passed on and analyzed. The surface detector IT consists of 81 stations, each 125 m apart. A photo of an IT station can be found in Figure 3.2. Each station is equipped with two ice-Cherenkov tanks, which have a distance of 10 m [16]. The individual tanks have an inner diameter of 1.86 m and are filled with 0.9 m of ice, in which there are two DOMs [5]. Both DOMs run at different gains, one at low gain and one at high gain. This extends the dynamic range [16], i.e. the range of particle counts that can be detected before saturation. There is a total number of 324 DOMs at IT [4]. A functional description of the DOMs can be found in a section below. The IT detectors need to be calibrated, and the calibration is performed with respect to a specific signal size. The reference unit used for the signal is Vertical Equivalent Muon (VEM). One VEM corresponds to the measured signal/the deposited charge of a vertical muon in an IT tank [17]. The constantly changing snow depth on the surface of IceCube (which is discussed more in detail in chapter 3.2.2) causes systematic errors in calibration.

The in-ice detector IceCube is located right under the surface array. It consists of a total of 5160 DOMs, which are connected to each other via 86 vertical strings [18]. In Figure 3.1, these strings can be identified as vertical lines. Each string is assigned 60 DOMs and the individual strings are arranged hexagonally [4]. To give a better idea of the order of magnitude: The strings are located between 1450 m and 2450 m depth and have a spacing of 125 m. The

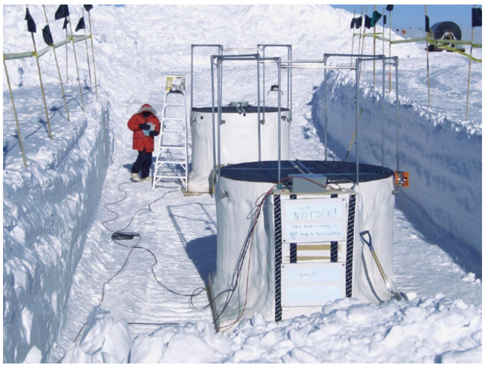

Figure 3.2.: Photo of an IT station. Two ice Cherenkov tanks are shown, which together form one IT station. Inside each tank, two DOMs are installed, which are responsible for detecting the Cherenkov light. The photo is taken from the IceCube Collaboration.

distances between the DOMs are 17 m [18].
In the center of the in-ice component, 8 strings have a smaller distance of about 70 m and the individual DOMs are only 7 m apart. This is shown in Figure 3.1 in the form of a compression of the strings. This compaction forms the so-called DeepCore sub-detector, which is used for the investigation of neutrino oscillations due to the reduced neutrino energy threshold of 10 GeV [4].

3.2.1 DOMs

The task of the DOMs is to collect Cherenkov photons and to acquire data. To fulfill these tasks, a DOM has the following main components: several circuit boards for data acquisition, control, digitization, calibration and communication and a down-facing Photo Multiplier Tube (PMT) [16]. All individual components are located in a spherical glass housing and a representation of them can be found in Figure 3.3. The circular main board handles most of the tasks already mentioned. The other components depicted in Figure 3.3 are responsible for generating PMT high voltage or for the connection to PMT pins. The flasher board is used to calibrate the individual DOMs by generating flashes of light which are then detected by other DOMs. The delay board delays the PMT signals [13]. In order for DOMs to detect particles of different energy ranges, they must also include various digitizers that can vary the sampling speed and have overlapping dynamic ranges. Last but not least, the DOMs are connected to each other and to the IceCube Laboratory via wire-pairs [16].

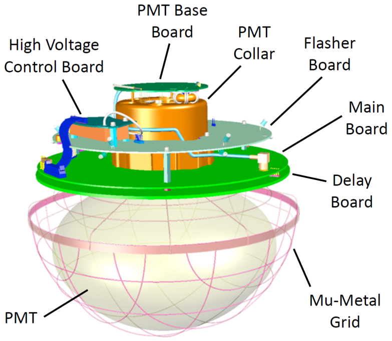

Figure 3.3: Schematic of a DOM. The individual components can be seen. Several circuit boards are located above a downward-facing PMT. Around the displayed components is a spherical glass casing. The depiction is from [13].

3.2.2 Surface Enhancement

The surface array of the existing IT will be expanded by what is known as surface enhancement. It was developed to improve IT as a cosmic-ray detector by using different types of detectors and boosting measurements, as well as being more cost-effective due to the type of the chosen detectors. They are scintillator detectors and radio antennas, leading to a hybrid surface detector system [2].
Choosing several types of detectors leads to an overall improvement, such as enhancing the capabilities to measure the mass composition of cosmic rays, extending the sensitive area, lowering the threshold due to a higher density of detectors or studying and understanding hadronic interactions [19]. The following aspects are specific to the selected detectors: Radio-antennas will help to increase the sensitivity to inclined showers, while scintillators can be used to improve the calibration of IT [16]. This is due to the fact, that they can be elevated above the snow which automatically avoids the snow accumulation that occurs at South Pole. Snow accumulation is a serious problem, as the calibration would have to be renewed due to the constantly changing snow depth. Placing detectors above the snow and keeping them snow-free reduces this problem and the scintillators can be used to calibrate the snow-covered Cherenkov-tanks of IT [2].

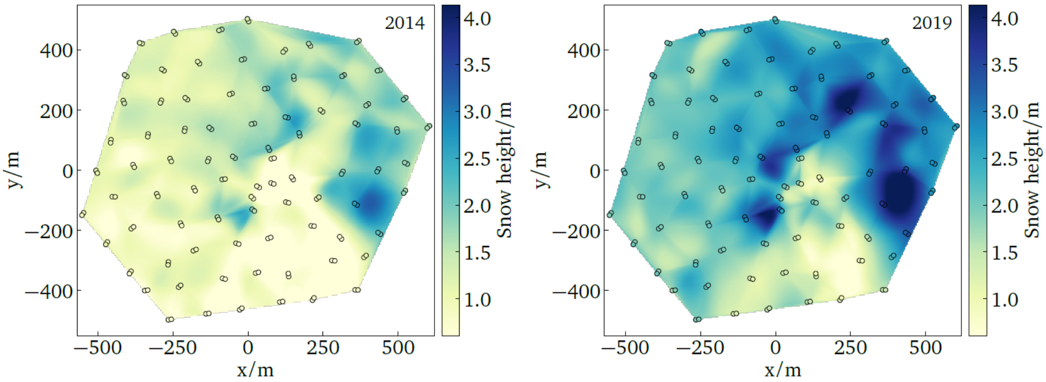

Figure 3.4.: Snow accumulation over a period of 5 years. Left: Snow height above the IT Cherenkov-tanks in March 2014. Right: Snow height above IT tanks in 2019. Plot is taken from [2].

Figure 3.4 illustrates how the snow height above the IT tanks changes over a period of 5 years. Most important things to notice here are on the one hand an increase in the snow height of about one meter and on the other hand a non-uniform accumulation. There are differences in height for about four meters, which means that the calibration also varies from tank to tank. One reason for the unevenly distributed snow height is that the tanks were not installed at the same time. First, the tanks in the upper right area were installed, resulting in a greater snow height there [2]. As the snow depth shown was also measured several years ago, it can be assumed that it has increased even more. The increase in snow height is about 20 cm/year on average [21].
Snow accumulation is the reason for the electromagnetic component of a shower being much more attenuated until it reaches the IT tanks. This in turn has the effect of increasing the threshold of the detector [16]. To prevent this, the scintillators are mounted above the snow cover. As they are made of lightweight materials, they are easy to install in an elevated position and can be kept snow-free [2]. A photo of a scintillator module at South Pole can be found in Figure 3.6.

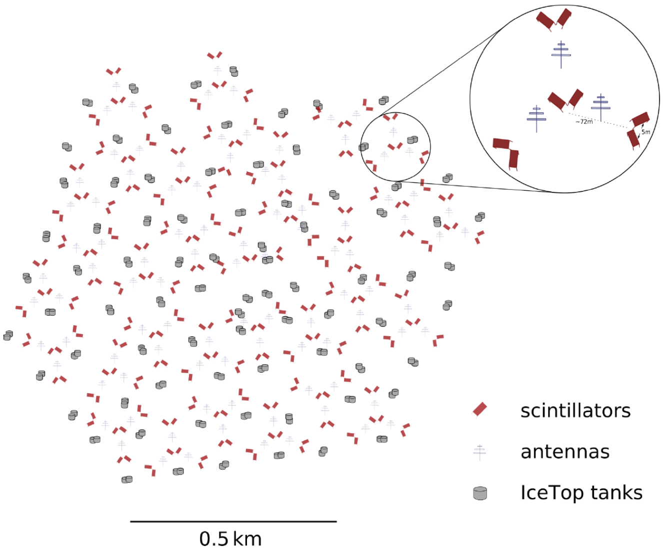

Figure 3.5.: Surface enhancement of the IT array. 32 stations with 8 scintillators and 3 radio antennas each are shown. The plot is taken from [20].

Figure 3.6.: Photo of scintillator module at South Pole. The panel is mounted in an elevated position to keep it snow-free. The photo to is taken from the IceCube Collaboration.

The layout for the surface enhancement of IT was planned in 2018/19. It consists of 32 stations with 8 scintillator detectors and 3 radio antennas each. The specific layout can be seen in Figure 3.5. It was chosen to achieve a uniform distribution of the scintillator panels [21]. A photo of a scintillator module in its elevated position at South Pole can be found in Figure 3.6. Since this work involves analyzing simulations of scintillator responses, the following section will focus on general knowledge about scintillators and the specific scintillator panels.

3.2.3 Scintillator Panels

Scintillator detectors are often used in particle physics to detect nuclear particles or radiation by creating scintillation light, which then can be, for example, converted to an electrical signal and can then be analyzed. Some of their positive characteristics are a fast time response,

sensitivity to the deposited energy and pulse-shape discrimination [22]. The first point mentioned provides a higher count rate of the ongoing events as other detectors and the second point means that the amount of produced light in a scintillator detector usually is proportional to the deposited energy, hence it provides information about the energy of the incoming particle. Different incoming particles create different shapes of scintillation light pulses, which helps identifying the type of the particle. This is called pulse-shape discrimination.
The main process in a scintillator, that produces the characteristic light, is caused by the incoming particle. It excites the molecules of the scintillator material and during the transition to the ground state, photons are emitted [2]. Organic scintillators, such as those used at IceCube, produce the scintillation light in transitions, which are made by free valence electrons of the molecules [22]. As the fluorescence process only takes place in single molecules, unlike inorganic scintillators, no crystal structure is required. Thus, fluorescence is independent of the physical state of the material [23].

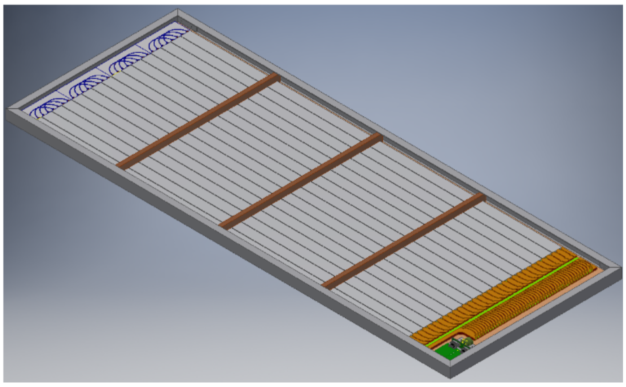

Figure 3.7.: Layout of a scintillator panel. It is shown without the cover so that the bars are visible. The bars are connected with wavelength shifting fibers, which are then connected to the Silicon Photo Multiplier (SiPM). To protect the equipment, an aluminum sheet about 1 mm thick is added [18]. Illustration is taken from [24].

The main components of the scintillator panels used at IceCube are 16 extruded plastic scintillator bars, wavelength shifting fibers and a SiPM. All components together have a weight of less than 50 kg, which enables to set them up easily [25]. The dimensions of the polystyrene bars are 5 cm × 1 cm × 187.5 cm, which gives a sensitive area of 1.5 m^2 per panel. To improve the properties of the bars, they are doped with 0.03 % POPOP and 1 % PPO. POPOP helps to shift the scintillator light to the correct range for the SiPM and PPO helps with producing scintillator light [2]. The bars are coated with a $\mathrm{TiO_2}$ layer with a thickness of 0.25 ± 0.13 mm [25]. An illustration of the scintillator panel is depicted in Figure 3.7.

As already mentioned in the beginning of this section, the scintillation photons need to be converted to an electrical signal for further analysis. This is done with photo-sensors, more precisely with the $6 \times 6\ \mathrm{mm}^2$ [24] SiPMs. SiPMs are built of pixels of Single-Photon Avalanche Diodes (SPADs) on a silicon substrate and some quenching resistors. An incoming photon creates an electron-hole pair in the silicon and thus triggers an electron avalanche. This avalanche becomes the electric signal and is stopped by the quenching resistors [26].
After the scintillators create some scintillation photons, that are converted to an electrical signal, the data must be processed further. The used data acquisition system is called IceTAXI. Each scintillator panel and corresponding SiPM is connected to a μ-Data Acquisition (DAQ)

board, which digitizes the signal before it is transmitted to the Scintillator Field Hub (SFH). The SFH is the DAQ node for one scintillator station and all SFHs are connected to the IceCube Laboratory [24].

3.2.4 IceCube Upgrade

Another extension in the ICNO is the so-called IceCube Upgrade to a low-energy core, which consists of seven [16] additional strings located near the existing DeepCore region inside the current array [4].
Unlike the outer strings, the Upgrade region features an increased string density within the in-ice detector. This configuration lowers the energy threshold to the GeV range and allows for a more effective discrimination of atmospheric muon background events. As a result, more precise observations of low-energy neutrino interactions become possible [20].
A total of 750 advanced photo-detectors will be installed, reaching depths of up to approximately 2500 m below the surface. Together with additional calibration devices, they will enable a better understanding of the light emission and propagation through the Antarctic ice [4]. With new and advanced versions of the existing DOMs, called Multi-PMT Digital Optical Module (mDOM) and Dual optical sensors in an Ellipsoid Glass for Gen2 (D-Egg), which are depicted in Figure 3.8, the photon detection efficiency and calibration capability of the detector increases [27]. Furthermore, the Upgrade will serve as a technological testbed for the future IceCube-Gen2 detector (see section 3.3), allowing to validate new sensor designs, calibration strategies, and deployment techniques under realistic Antarctic conditions.

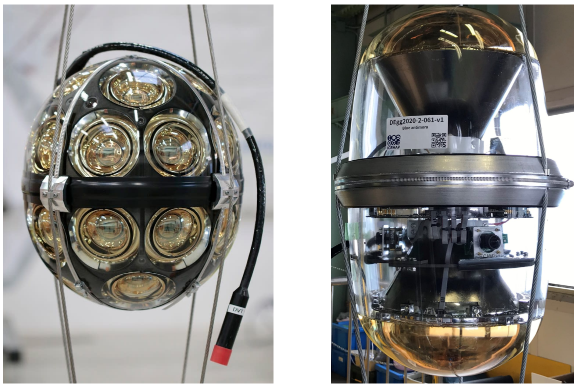

(a) (b)

Figure 3.8.: Photograph of the mDOM (a) and D-Egg (b) optical modules developed for the IceCube-Gen2 detector. Both designs feature multiple photomultiplier tubes to increase detection efficiency and calibration capability. Credits: DESY (a) and ICEHAP (b).

3.3 IceCube-Gen2

Following the achievements of the current IceCube detector, the next-generation observatory, IceCube-Gen2, is planned to expand the instrumented volume. The goal is to provide, besides the larger detection volume, a higher sensitivity, sharper resolutions, as well as a better understanding of the properties of neutrinos in general [4]. To achieve this, there are new extensions: an in-ice radio array, an in-ice optical array, as well as a surface array [20]. A 3D-visualization of the planned extensions can be seen in Figure 3.9. IceCube-Gen2 will contain many more strings that will have a larger distance between them. The current distance between two strings is 125 m, but will increase to around 250m for IceCube-Gen2 [4]. The optical sensors are also upgraded. Instead of the usual DOMs, there will be new ones having lower power consumption and higher sensitivity. Each of the 120 new strings will contain 80 of the new DOMs [16].

The advantages of the new arrangement and the new elements are wide-ranging. First of all, larger spacings between the strings is increasing the detector volume without reducing the sensitivity of the DOMs to Cherenkov light. Studies of the properties of Antarctic ice have shown that the absorption length of Cherenkov light is greater than the 100 - 200 m previously assumed [18]. At this point, however, it should be noted that the larger spacing also has a negative effect, as it raises the energy threshold and reduces the directional resolution. In order to keep these negative effects within a manageable range, the spacing of the strings was ultimately set at the 240 m already mentioned [28], i.e. optimized for the detection of astrophysical neutrinos in the energy range of $10^{15} - 10^{18}$ eV.

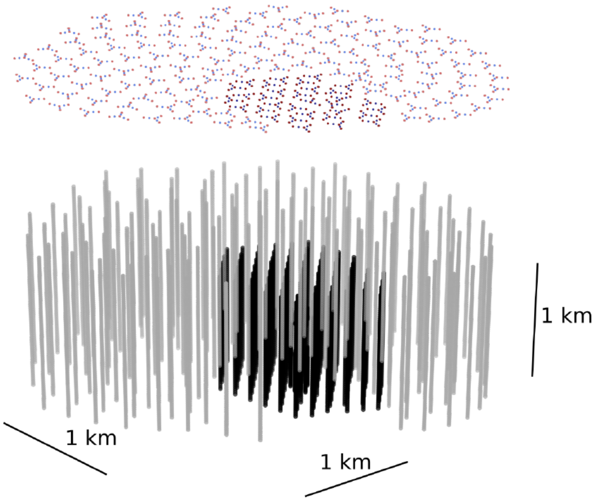

Figure 3.9.: Rendering of the planned IceCube-Gen2 components. The gray strings represent the planned optical array, while the black strings show the current IceCube configuration. In the middle of this black area, seven [16] new strings are planned, which belong to the IceCube Upgrade (low-energy core). Above the strings, the planned surface detectors are visualized. The image is taken from [29].

Part of the IceCube-Gen2 upgrade is a further enhanced surface array. It will increase the veto capabilities which helps to decide between background events and cosmic rays [20]. For this, the existing IceCube surface enhancement is used and extended to an even larger area. As becomes visible in Figure 3.9, the IceCube-Gen2 strings and surface array are chosen to have a 'sunflower' geometry.

After discussing the basics of CR physics and the components of the IceCube Neutrino Observatory, the focus will now shift to the analysis of two aspects of the upgrade, namely the scintillator stations and the IceCube Upgrade. To asses the potential of these extensions, a multiple step analysis is performed, starting with the efficiency of the scintillator stations.

4 Efficiency of Three Scintillator Stations

Efficiency is a key parameter for evaluating detector systems. It indicates the probability that an event with a certain primary energy will trigger the detector and thus be detected and reconstructed by it. This chapter therefore explains the basics and the methodological determination of efficiency and its significance. In this thesis, the consideration of efficiency is limited to the scintillator detector type. More precisely, efficiency is only determined for three of the planned scintillator stations. The reason for this is that two of these three stations, namely station 21 and 25 (see Figure 4.1), have newly been installed. Station 16 is also included in the simulation studies because it is very close to the location of the very first operating prototype station and it is located directly near stations 21 and 25. A general overview of the scintillator array can be found in Figure 4.1, whereby the exact position of the stations in question is additionally marked. It should be noted that the coordinates used in the analysis, which are based on the planned layout, may slightly differ from the coordinates of the actual detector deployment.

For the purpose of determining the efficiency, a simulated dataset created specifically for the analysis of scintillator responses is used. The dataset was developed for the purpose of investigating the potential of the IT surface array enhancement in [2]. The simulation chain includes the simulation of an atmospheric cascade started by a primary particle. With the information of the distribution of particles at the observational level, the next step is to propagate the secondary particles through the detectors and to create signals [2].
The simulation used in this analysis contains a primary energy range from 10^{12} to 10^{17} eV for different primary types. This work will focus on proton (H) and iron (Fe) as primary particles. The zenith angle range for incoming particles is from $0°$ to $50°$, the azimuth angle range from $-180°$ to $180°$. For energies below 80 GeV, within COsmic Ray SImulations for KAscade (CORSIKA) [30], the simulation program, the hadronic interaction model FLUKA is used, for high-energy interactions SIBYLL 2.3c is used. More key parameters can be found in the appendix section A.

4.1 Sampling Area

The efficiency is calculated for a so-called sampling area. This defines a specific area of the scintillator array from which data is used for the calculation. Throughout the analysis, multiple versions of the sampling area were created, which all can be seen in Figure 4.1. The sampling area on the right-hand side (b) was used as a first approximation. It consists of two rectangles and is therefore referred to as rectangular sampling area. The results for variations of this initial sampling area can be found in appendix B. The smaller area on the left hand side (a), labeled 'Sampling Area Oval' represents the final chosen region. It covers an area of 45337.17 m^2, which corresponds to 5.77 % of the whole surface array approximated by a circular area with a radius of 500 m. For later comparison, a second, larger version is shown (dashed line), which corresponds to the same area extended by a 50 m padding.

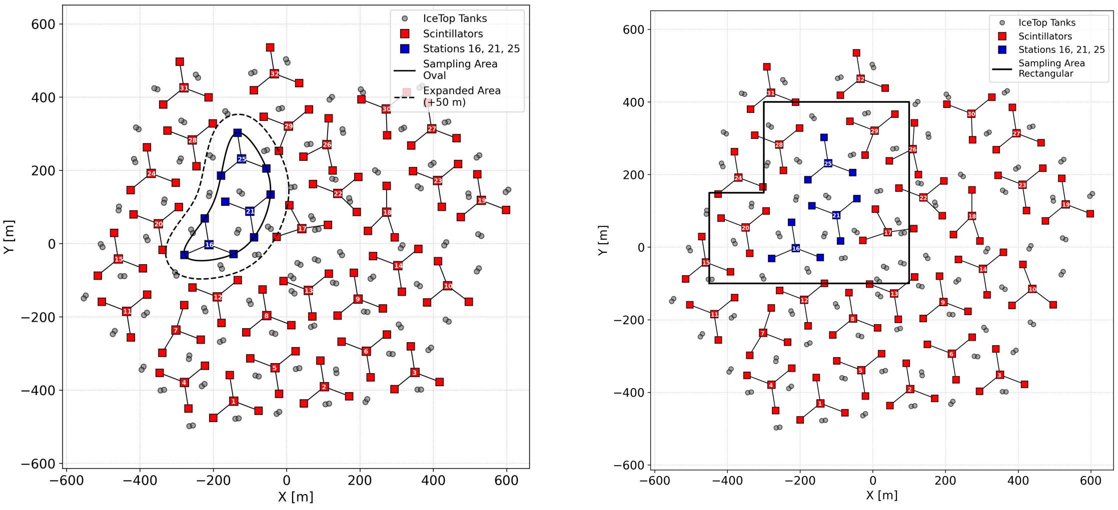

(a) **(b)**

Figure 4.1.: Scintillator array and sampling areas. Both plots show the 32 stations with 4 scintillator-panel-pairs each. The stations 16, 21, and 25 used for the analysis are colored blue. Different possibilities for the sampling area are shown in black. The oval, or more likely banana-shaped area (a) is the final area and the rectangular area (b) was initially used.

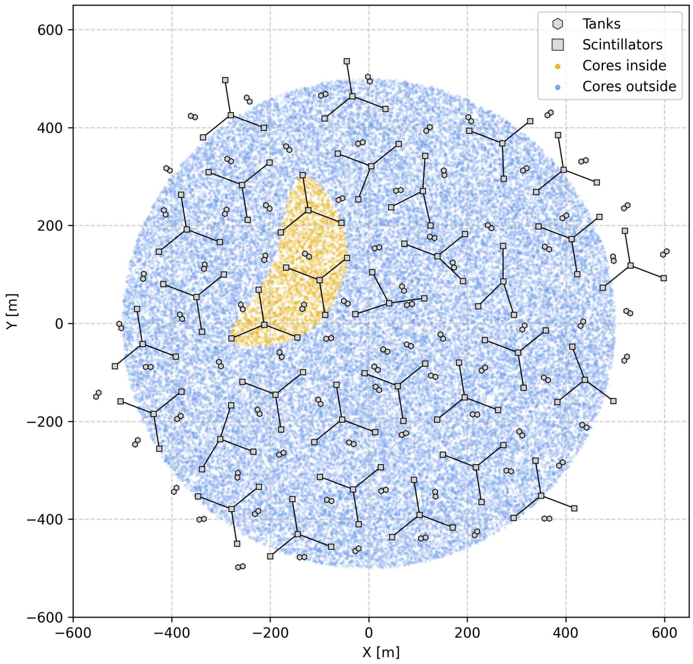

Figure 4.2: Core positions of proton-induced showers with $\theta < 25.84°$. Showers that land inside the sampling area are used for further efficiency analysis and are colored in yellow. The

The difference that the choice of sampling area makes becomes clear with the definition of efficiency in equation 4.1.

$$\varepsilon = \frac{N_{trigger}}{N_{total}} \tag{4.1}$$

N_{total} is the number of events/showers that land within the sampling area just mentioned and satisfy the condition $\cos\theta > 0.9$,i.e., events in which the zenith angle of the primaries satisfies $\theta < 25.84°$. $N_{trigger}$ is the number of showers that, in addition to the conditions of N_{total}, also fulfill further trigger conditions, which will be mentioned later.

If the sampling area is chosen generously around the three stations, the number N_{total} would increase. However, these additional events do not necessarily meet the trigger conditions, which in turn changes the final efficiency curve. An increase in the defined area does not imply a loss of validity, it simply corresponds to a different operational definition of efficiency. In this work, the focus is on placing the sampling area as close as possible to the scintillator stations.
A visualization of the proton showers used for the calculation of the efficiency in the oval sampling area, thus proton showers that are included in N_{total}, is depicted in Figure 4.2. Although showers outside the sampling area could also meet the trigger conditions (see section 4.2), the cut to the sampling area is applied first.

The efficiency is calculated for a group of primaries. The primaries are grouped according to their primary energy, which is referred to as different energy bins. The energy bins are specified in the unit $\log_{10}(E/\mathrm{GeV})$ and have a width of 0.2 $\log_{10}(E/\mathrm{GeV})$. For each energy bin, the error is calculated using the following equation [14].

$$\sigma_\varepsilon = \sqrt{\frac{(N_{trigger}+1)(N_{trigger}+2)}{(N_{total}+2)(N_{total}+3)} - \frac{(N_{trigger}+1)^2}{(N_{total}+2)^2}} \tag{4.2}$$

N_{total} and $N_{trigger}$ refer to the respective number of events in the corresponding energy bin.

4.2 Trigger Conditions

In the context of this work, the trigger conditions relating to the pulses generated in the scintillator panels were chosen as follows:

- threshold for pulse charge of 0.5 MIP per scintillator panel
- ignoring pulses from the same pair of panels
- minimum number of hit pairs of panels

The first condition ensures that only events whose pulses have a charge greater than 0.5 MIP are considered. Minimum Ionizing Particle (MIP) describes a particle that loses only the minimum possible energy when passing through matter, i.e., has the smallest energy deposition [14]. This corresponds to the threshold of the scintillator panels. The second condition ensures that only pulses measured at different locations in the scintillator station are considered. The reason for this is that two pulses coming from the same branch of the station provide information that hardly differs.
The last condition is a variable condition that is always based on a certain number of minimum hits and combines the first two conditions. A hit is counted as such if at least one pulse with a charge above the discriminator threshold is registered on a panel pair. Since the scintillator stations are arranged with 8 panels each in 4 panel pairs, the maximum possible number of hits per station is 4. The number of minimum hits specifies how many hits must be counted at least across all three stations. It doesn't matter how the hits are distributed across the three stations, as long as this minimum number is reached in total. If a shower leaves at least this number of hits, it counts as 'triggered' and $N_{triggered}$ increases by this shower.

4.3 Efficiency Results

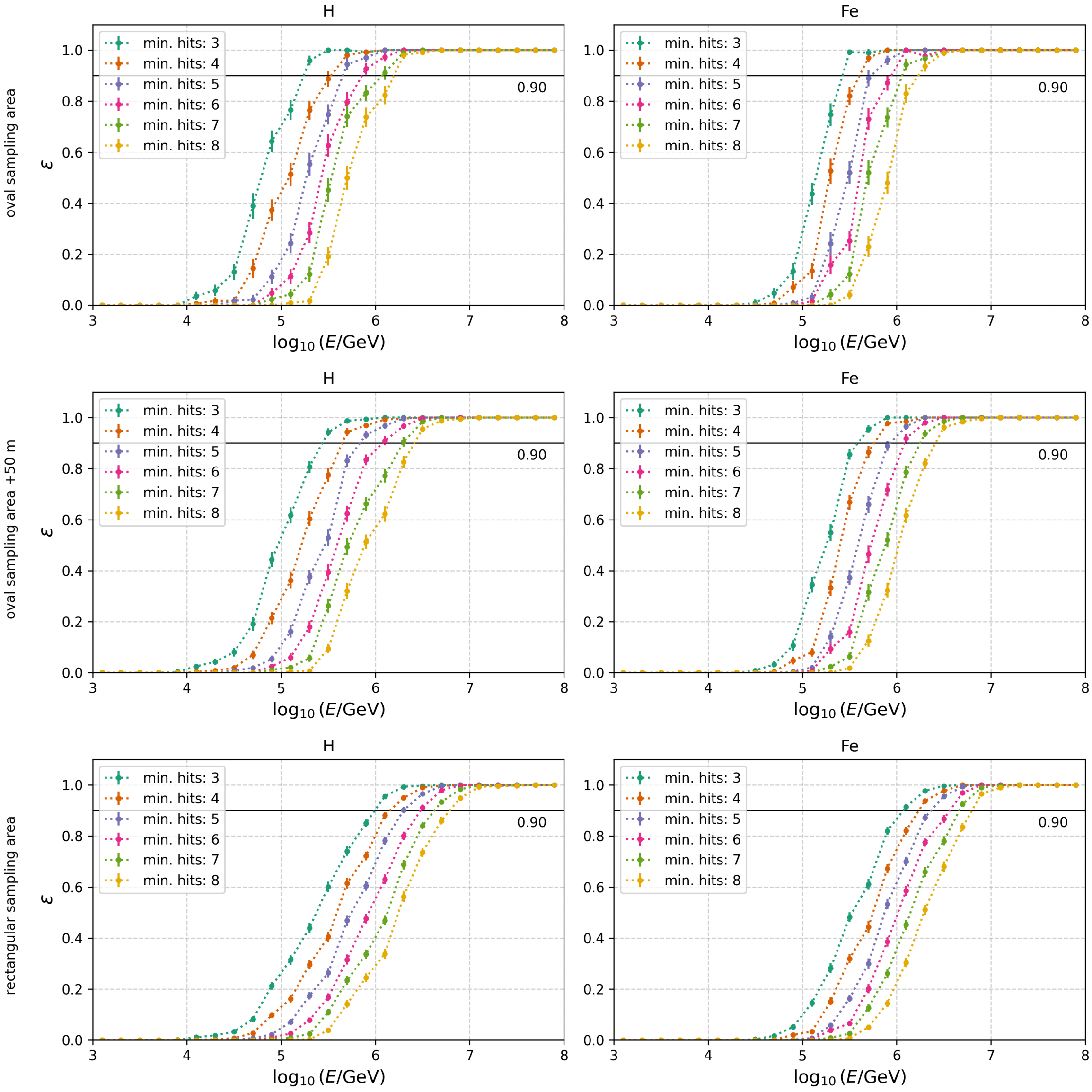

Figure 4.3.: Efficiency ϵ for three scintillator stations and different sampling areas as a function of the primary energy. The left hand side plots are for proton showers, the right hand side show the efficiency curves for iron. The rows represent the efficiency for different sampling areas, which are described in Figure 4.1. The curves within a plot represent a different number of minimum hits.

The plots in Figure 4.3 show the efficiency of the three stations as a function of the primary energy. Different conditions for the number of minimum hits are shown in each plot. The efficiency is calculated both for the different primary types and different sampling areas. The smaller the number of minimum hits, the higher the efficiency for the same primary energy. Using the 90%-efficiency as a reference, the following statements can be made for the proton-(iron-)induced shower. For the oval sampling area, the curve for five minimum hits reaches 90%-efficiency at an energy of approximately 5.65 $\log_{10}(E/\mathrm{GeV})$ (5.73 $\log_{10}(E/\mathrm{GeV})$). If the trigger condition is at least three hits, the 90%-efficiency is already achieved at primary energies of 5.24 $\log_{10}(E/\mathrm{GeV})$ (5.42 $\log_{10}(E/\mathrm{GeV})$). With iron, the efficiency is slightly lower in each case. This is because an iron-induced shower has its first interaction in the atmosphere earlier than proton, as it was discussed in equation 2.10. As a result, the secondary particles are distributed much more widely [2], and fewer particles arrive at the scintillators. This decreases the probability that a shower will meet the trigger conditions, which is ultimately reflected in the lower efficiency.

In all cases, a plateau is reached, i.e., above certain energies, all events trigger the scintillators. With a minimum of 3 hits, this is already achieved at approximately 5.5 $\log_{10}(E/\mathrm{GeV})$ (5.42 $\log_{10}(E/\mathrm{GeV})$), with a minimum of 8 hits at approximately 6.70 $\log_{10}(E/\mathrm{GeV})$ (6.23 $\log_{10}(E/\mathrm{GeV})$).

sampling area	$E_{90\%,\mathrm{H}}$ **[$\log_{10}(E/\mathrm{GeV})$]**	$E_{90\%,\mathrm{Fe}}$ **[$\log_{10}(E/\mathrm{GeV})$]**
oval	5.24	5.42
oval extended	5.44	5.59
rectangular	5.99	6.07

Table 4.1.: Energies corresponding to 90%-efficiency for different sampling areas. The values apply to the trigger condition of three minimum hits.

Table 4.1 allows for a direct comparison of the efficiency for different sampling areas. The energy, at which the 90% efficiency for at least three hits is achieved, is used as the comparative value. It becomes evident that the larger the sampling area, the higher the energy at which 90% efficiency is achieved. This is due to the higher number of showers considered in N_{total}. It once again illustrates the influence that the choice of sampling area has.

The efficiency analysis demonstrates the dependence of the efficiency on both the sampling area and the trigger configuration. When the sampling area is chosen close to the detector stations, high efficiency is already reached at lower primary energies. If interested in higher energies above 10^{16} eV, one can extend the targeted area and still have full efficiency.

I.e., the area and minimum hits condition can be optimized depending on the goal of the analysis. For this, the presented study provides guidance for the determination.

In addition, the determined efficiency curves provide a reference for interpreting future measurement data with the three-station setup. The results show how efficiency changes with primary energy and geometric conditions, enabling a more accurate estimation of the detector acceptance and exposure in real data analysis.

5 Reconstruction

To analyze the observed information from CRs, a reconstruction using the observables is important, and its performance is therefore a part of the analysis conducted within this thesis. While performing a reconstruction, important properties of the incoming CR, such as its core position, energy, or the direction from which it hits the detector, are determined using the available pulse information from the detectors, i.e., charge and timing information. With a reconstruction, statements about the primary particles can be made.

In this work and many other works within the IceCube experiment, the reconstruction algorithm *RockBottom* [31], which is part of the IceCube software, is used for this purpose. *RockBottom* has been continuously developed over time, so that multi-detector reconstruction is now possible, i.e., a reconstruction that combines IT and in-ice data [2].

The reconstruction utilizes the pulse and timing information by performing fits to the lateral distribution of the pulses and the time of arrival of these pulses at the detectors. These fits are optimized by using the minimized negative log-likelihood method [31].

Before the specific likelihood-terms used for the actual reconstruction are introduced, the general principle of likelihood functions and minimization of the negative log-likelihood is explained first.

5.1 Principles of Negative Log-Likelihood Minimization

The goal of a statistical analysis is often to fit a suitable model function to given data in order to describe it. However, sometimes several distributions with different parameters can provide such a description. Therefore, the goal is to find the best possible distribution. The likelihood function $\mathcal{L}$ helps in doing that. It is a measure of how well the parameters of a distribution fit the given data. $\mathcal{L}$ is a function of the probability distribution that is characterized by the parameters Θ, whereby the observed data is considered to be given. This is also written as $\mathcal{L}(\Theta \mid \text{data})$.

The likelihood is the probability density of all N events $\vec{x}$, which is given by the product of the probabilities of the individual events x_i.

$$\mathcal{L} = P(\vec{x} \mid \Theta) = \prod_{i=0}^{n} P(x_i \mid \Theta) \tag{5.1}$$

Since the individual probabilities are usually very small, the product of the probabilities becomes even smaller, which can lead to incorrect calculations due to rounding errors. Therefore, the log-likelihood is used. It converts the product of the individual probabilities according to

$$\log(AB) = \log(A) + \log(B) \tag{5.2}$$

into a sum [32]. The search for maximum likelihood gives the parameters that best fit the data. In practice, minimizing the negative log-likelihood is usually used instead of maximizing the likelihood.

5.2 Specification of the Signal Distributions

As already mentioned, a Lateral Distribution Function (LDF) and a timing model are fit to the measured data during reconstruction. The reason for this is that these models provide information about characteristics of the shower. The LDF describes how the secondary particles are distributed around the core or shower axis. This description of the particle density is used to determine the core position of the shower. There is also a correlation with the primary energy and the type of primary particle.

The timing model is used to describe the curvature of the shower front. As already shown at the beginning of this work in Figure 2.2, the description of the shower front as a plane is only an approximation. In fact, the shower front is slightly curved, i.e., the secondary particles arrive at the detector with a time delay. This is precisely what the timing model describes: the delay of the arrival times of the signal with respect to the arrival time of the shower plane [2]. The distribution of these delays provides e.g. information about the direction of incidence of the shower or its core position.

5.2.1 Lateral Distribution Function

The basis of the LDF used in the reconstruction is the approximation of lateral density by J. Nishimura and K. Kamata [33] and K. Greisen, also known as the NKG function. It is a function of the distance to the shower axis r and is given by

$$\rho_{NKG}(r) = \frac{N_e}{2\pi r_m^2} \frac{\Gamma(4.5-s)}{\Gamma(s)\Gamma(4.5-2s-2)} \left(\frac{r}{r_m}\right)^{s-2} \left(1+\frac{r}{r_m}\right)^{s-4.5} . \tag{5.3}$$

N_e describes the number of all electrons at the observational level, r_m is the so-called Molière radius. It is a material-dependent constant defined by considering an imaginary cylinder around the shower axis. It corresponds to the radius of the cylinder that contains 90% of the energy of the electromagnetic shower [34]. At South Pole it corresponds to 128 m [2]. Γ is the gamma function and the slope parameter s describes the development of the shower, more precisely the slant depth, up to which the shower reaches the ground.

The Double Logarithmic Paraboloid (DLP) function is an empirical approximation which describes the same qualitative behavior of the air showers as the NKG function. It was found to be suitable for the reconstruction of IT signals, but it is also suitable for the reconstruction of the scintillator array [2]. It is therefore also used in the reconstruction of this thesis and describes the dependence of the signal S on the lateral distance r, thus $S(r)$.

$$S_{DLP}(r) = S_{ref} \left(\frac{r}{R_{ref}}\right)^{-\beta-\kappa \log_{10}\left(\frac{r}{R_{ref}}\right)} \tag{5.4}$$

Taking the logarithm of this gives the double-logarithmic paraboloid function, also known as the loglog-function, to

$$\log_{10}(S_{DLP}(r)) = \log_{10}(S_{ref}) - \beta \log_{10}\left(\frac{r}{R_{ref}}\right) - \kappa \log_{10}^2\left(\frac{r}{R_{ref}}\right). \tag{5.5}$$

β can be considered as the slope of the LDF. R_{ref} is a reference distance set to R_{ref} =125m and S_{ref} is the corresponding signal strength.

5.2.2 Time Front Model

At the start of the reconstruction chain, the shower front is approximated as a plane disc. This approximation is optimized by describing a curved disc. The functional relationship used for this in *RockBottom* for IT reconstruction [2] is given by an exponentially modified parabola.

$$\Delta t(r) = d\left[\exp\left(-\frac{r^2}{f^2}\right)+1\right]-gr^2 \tag{5.6}$$

d, f and g are given shower front parameters and r is again the lateral distance of the secondaries to the shower axis.
The time model for scintillator reconstructions is a simple parabola as given in equation 5.7.

$$\Delta t(r) = gr^2 + t_0 \tag{5.7}$$

Since this analysis reconstructs events on basis of the scintillator data, the simple parabola model is used for this purpose.

5.3 Specification of the Likelihood Terms

In order to optimize the signal distributions, the corresponding log-Likelihoods are minimized. For the optimization of the LDF, the following log-likelihood must be considered:

$$\ln \mathcal{L}_{LDF} = \ln \mathcal{L}_{tr} + \ln \mathcal{L}_{sa} + \ln \mathcal{L}_{si}\,, \tag{5.8}$$

where $\mathcal{L}_{tr}$ is the likelihood for triggered detectors, $\mathcal{L}_{sa}$ for saturated detectors and $\mathcal{L}_{si}$ for silent detectors. The individual log-likelihoods are as shown below.
The following applies to triggered detectors

$$\ln \mathcal{L}_{tr} = \begin{cases} -\sum_i \left[\frac{1}{2}\left(\frac{S_i - S_{LDF_i}}{\sigma_i}\right)^2 + \ln\left(\sqrt{2\pi}\sigma_i\right)\right], & \text{if } S_i \geq 2 \text{ VEM} \\ -\sum_i \left[S_{LDF_i} - S_i \ln\left(S_{LDF_i}\right) + \ln\left(\Gamma(S_i+1)\right)\right], & \text{if } S_i < 2 \text{ VEM}, \end{cases} \tag{5.9}$$

where S_i is the signal from the i^{th} detector. S_{LDF} is then the signal predicted by the LDF used, and σ_i is the square root of the signal variance. There is a case distinction here, which is defined by the strength of the signal. If the signal falls below 2 VEM, then the signal no longer corresponds to a Gaussian distribution, but is instead described by a Poissonian function.
For saturated detectors, the log-likelihood corresponds to

$$\ln \mathcal{L}_{sa} = \sum_i \ln\left[\frac{1}{2}\operatorname{erfc}\left(\frac{S_{max} - S_{LDF_i}}{\sqrt{2}\sigma_{sa_i}}\right)\right]. \tag{5.10}$$

It contains the complementary error function, and σ_{sa_i} is also the square root of the signal variance, and S_{max} is the signal value of the detector at saturation.
For silent detectors, i.e., detectors that have not registered a signal, the log-likelihood is represented by

$$\ln \mathcal{L}_{si} = \sum_i \ln\left(1 - P_{hit}\right). \tag{5.11}$$

P_{hit} is the probability that a detector is triggered. In this case, the trigger condition is that the signal must be greater than or equal to the value 0.5 VEM. The probability P_{hit} is specifically defined by

$$P_{hit} = 1 - a\left(1 + \mathrm{erfc}\left(\frac{b - \log_{10}(S_{LDF_i})}{c_1}\right)\right)\left(1 + \tanh\left(\frac{b - \log_{10}(S_{LDF_i})}{c_2}\right)\right) . \tag{5.12}$$

For the optimization of the time parabola, the timing log-likelihood is

$$\ln \mathcal{L}_t = -\sum_i \sqrt{S_i}\left[\frac{1}{2}\left(\frac{\Delta t_i - t_{front_i}}{\sigma_{t_i}}\right)^2 + \ln(\sqrt{2\pi}\sigma_{t_i})\right] . \tag{5.13}$$

Δt_i is used for the measured arrival times by the i^{th} detector and t_{front_i} corresponds to the arrival time expected by the shower front model. σ_t stands for the time spread resulting from the shower thickness.

All these log-likelihoods are combined during reconstruction to form a likelihood $\ln \mathcal{L}$, as can be seen in the following equation 5.14.

$$\ln \mathcal{L} = \ln \mathcal{L}_{tr} + \ln \mathcal{L}_{sa} + \ln \mathcal{L}_{si} + \ln \mathcal{L}_t \tag{5.14}$$

This combination of all likelihoods enables a comprehensive reconstruction that takes into account both charge and timing information. The reconstruction process consists of three steps in which different parameters are either free or fixed. The ranges of the free parameters are varied to allow for optimization. In the first step, only the charge information is used. In the second step, both charge and timing information are included and in the third and final step, only the charge information is considered again.
One objective of this work is to perform and analyze the reconstruction for the detector response of the scintillator stations. This was done for the scintillator stations 16, 21, and 25. In the further course of the work, the results of the reconstruction will be evaluated with regard to their ability to correctly reconstruct the true primary. One method of assessing this is to calculate the resolution of a reconstruction.

5.4 Definition and Determination of Resolutions

In the frame of this thesis, two types of resolution are discussed: angular resolution and core resolution. They are defined in more detail in the following sections, and the respective results of the reconstruction are then presented. Finally, a comparison is made between the results of this work and the results of a reconstruction based on only one scintillator station. The purpose of this comparison is to highlight how the resolution improves when increasing the number of scintillator stations from one to three.

5.4.1 Core Resolution

The first reconstructed parameter to be examined in more detail is the core resolution. It shows how well the core position of a shower is reconstructed. The difference between the true shower core position and the reconstructed core position is referred to as Δr. This is calculated for all the events in an energy bin. For the resolution, the energy bins have a width of 0.1 $\log_{10}(E/\text{GeV})$. In the first step, Δr is calculated for each event and the resulting distribution is plotted per energy bin. These plots can be found in the appendix in section C.1 and C.2. The core resolution of an energy bin is defined as the 68th percentile of the Δr distribution. The 68-percentile corresponds to the value at which 68% of the measurements in a distribution are smaller than or equal to this value [35].
The uncertainty of the resolution is calculated using the bootstrap method [36]. The starting point is the distribution of the Δr values and their 68-percentile. This distribution is resampled by drawing random values from the given distribution with replacement. This resampling step is performed N times (here N = 10000). For each of these samples, the 68-percentile is calculated again. This yields N values for the 68-percentile of an energy bin. In the next step, the 95% confidence interval is calculated from these sampled 68-percentiles, i.e., the range in which the true value lies with 95% probability. With the assumption of the distribution of the sampled 68-percentiles being symmetric, the error can be approximated as half the width of the 95% confidence interval.

5.4.2 Angular Resolution

The angular resolution is calculated using a similar procedure, except that instead of Δr, the space angle α is calculated. In the context of reconstructing simulated data, the space angle is the angle between the true simulated shower direction $\vec{n}_{true}$ and the reconstructed direction of the shower $\vec{n}_{reco}$.

$$\cos(\alpha) = \frac{\vec{n}_{true} \cdot \vec{n}_{reco}}{\left|\vec{n}_{true}\right| \cdot \left|\vec{n}_{reco}\right|} \tag{5.15}$$

The angular resolution is again derived from the 68th percentiles of the underlying distributions, which are calculated using equation 5.15, and the uncertainties are determined using the bootstrap method as well.

5.5 Three-Station Reconstruction Resolutions

The following quality cuts apply to the events used for calculating the resolutions of a reconstruction based on three scintillator stations. On the one hand, only showers with $\theta \lesssim 26°$ are considered and on the other hand, the status of the reconstruction must be OK. This is a flag in the *RockBottom* framework that indicates that the log-likelihood minimization was successful. Furthermore, the shower must have at least three hits as defined in Chapter 4. These conditions apply to all resolution plots shown. However, different conditions were also specified for the core position of the showers used, which is why there is a variation in the different plots.

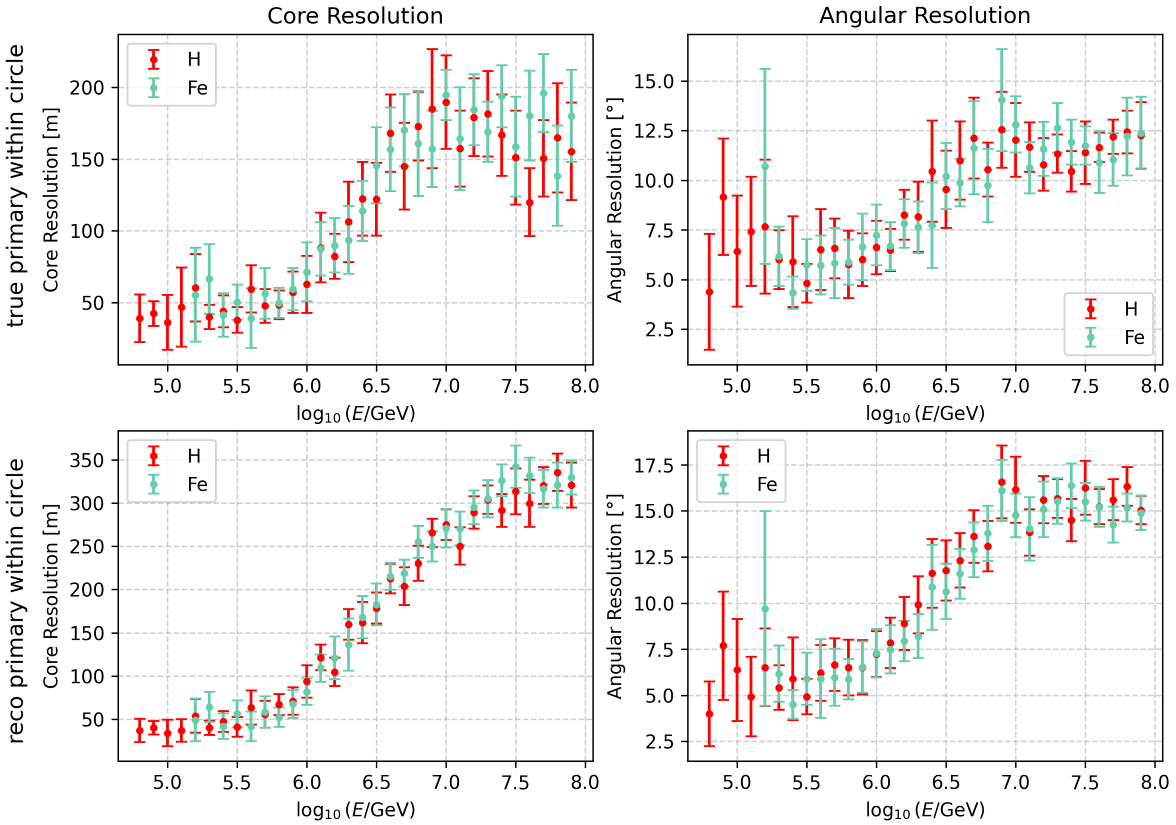

Figure 5.1.: Resolutions for cores in a circular area with $r = 300$ m around the center of the array as a function of the primary energy. This condition is applied on the true core positions (first row of plots) and on the reconstructed core positions (second row of plots). Both core resolution and angular resolution are shown for the given quality cuts.

The plots in Figure 5.1 show the resolutions for primaries where the true core position or the reconstructed core position fall within a circle around the center of the array with a radius of 300 m. The curves look similar for both protons and iron. While the core resolution at lower energies of around 5.0 $\log_{10}(E/\text{GeV})$ is still below 50 m, it increases from around 6.0 $\log_{10}(E/\text{GeV})$ and ends in the case of the true core within the defined circle at a core resolution of up to 200 m. The angular resolution varies in the bins shown between approximately 4° and 13°. The degradation in resolution with increasing primary energy can be explained by the constraints imposed by the reconstruction and resolution setup. While the area of the accepted shower cores is generously selected, the reconstruction itself is based on only three stations. At low energies, the distribution of secondary particles remains more compact, so that mainly showers with cores located close to the three stations are able to trigger. At higher energies, the secondary particles are distributed much more widely and, due to their higher energy, can still trigger the stations even at greater distances. This leads to larger deviations from the core and direction and to an increase in the resolution values.

It also becomes evident that the resolution degrades even further when, instead of the true core, the reconstructed core is required to lie within the circular area. This effect arises because the uncertainty of the reconstructed core is now included. For example, events whose true core actually lies outside the acceptance region may still be considered if they are mistakenly localized within the circle by the reconstruction. Such misreconstructions contribute to larger deviations and therefore to a further degradation of the resolution.

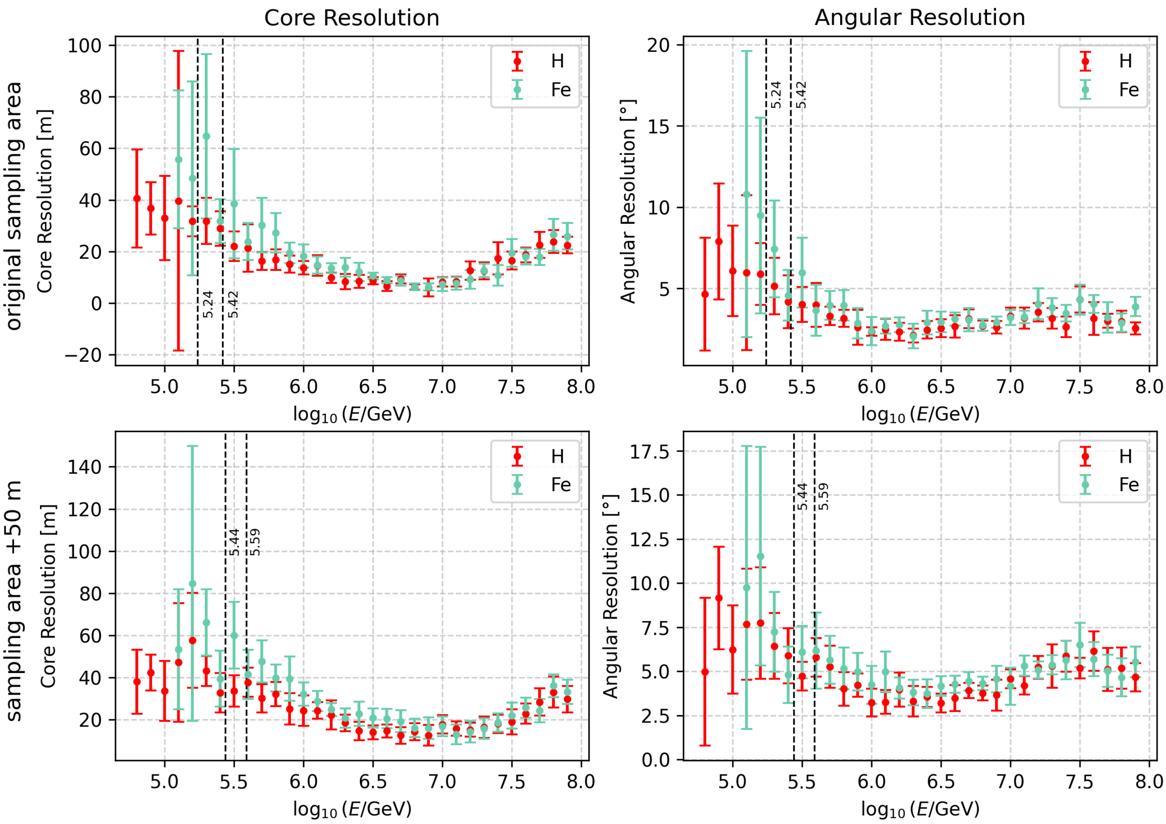

Figure 5.2.: Resolutions for cores in sampling area (upper panels) and sampling area with a padding of 50 m around it (lower panels) as a function of the primary energy. Both core resolution and angular resolution are shown for the given quality cuts. Vertical lines show the energies, at which 90%-efficiency is achieved for at least 3 hits. The lower value always corresponds to proton, the higher value to iron.

For the resolution in Figure 5.2, the condition for the true core positions was chosen differently. The reference area is now the oval sampling area that was already used for the efficiency (see Figure 4.1 (a)). The top row of plots shows the resolutions for showers whose true core position lies within this area. The bottom row of plots uses the sampling area extended by 50 m as the reference region.
In comparison to Figure 5.1, the resolutions are now significantly better, since only events are considered that land close to the stations actually used for the reconstruction. A comparison of the plots within Figure 5.2 also shows that the best possible resolution is achieved when the reference area is chosen as small and as tightly around the used stations as possible. In this case, the following statements can be made about the core resolution. Both proton and iron primaries achieve their best core resolution at 6.9 $\log_{10}(E/\text{GeV})$ with 6.08 ± 3.40 m (H) and 6.23 ± 1.41 m (Fe). The best angular resolution is reached for both proton and iron at 6.3 $\log_{10}(E/\text{GeV})$ with 2.09 ± 0.44° (H) and 2.05 ± 0.76° (Fe).
In Figure 5.2, vertical lines indicate the energies at which 90% efficiency is reached for a minimum of three hits (see Chapter 4). The corresponding core resolution values of the nearest energy bins are 31.71 ± 5.80 m ($E = 5.2 \log_{10}(E/\text{GeV})$, H) and 31.76 ± 8.54 m

(E = 5.4 $\log_{10}(E/\text{GeV})$, Fe). The angular resolutions in the same energy bins are 5.88 ± 3.16° (H) and 4.56 ± 1.60° (Fe), respectively.

5.6 Single-Station Reconstruction Resolutions

To illustrate the impact of considering only one station instead of three, the resolution was recalculated for a reconstruction based on only one station. For this purpose, the simulation of the prototype station located near station 16 was used[1]. The selected area to which the events used for this calculation are restricted is a circular region with a radius of 100 m around the central scintillator panel pair. All other quality cuts were kept identical, including the requirement of at least three hits, which ensures the best possible comparison.

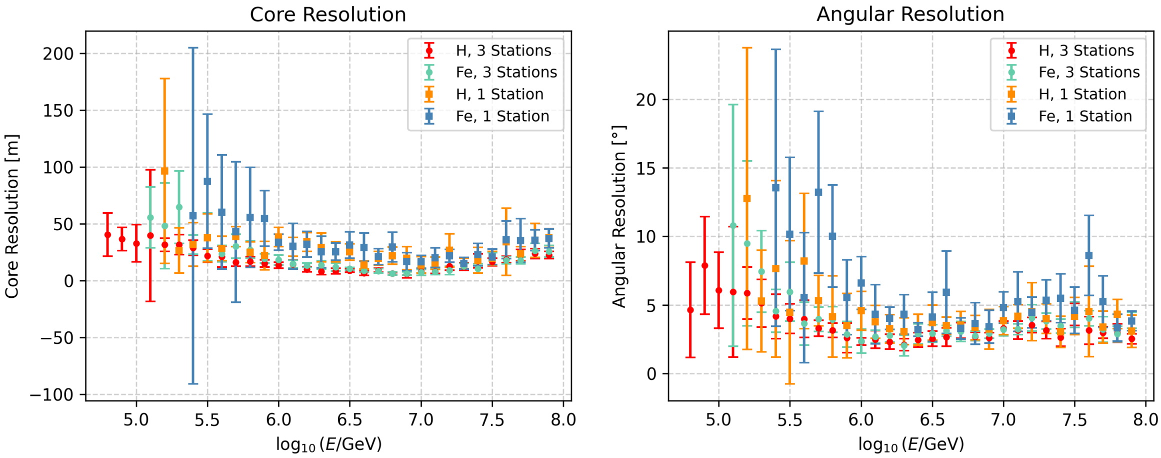

Figure 5.3.: Resolutions for prototype station as a function of the primary energy. Both core resolution and angular resolution are shown for showers landing in a circular area around the center of the prototype station with radius 100 m, and with the remaining cuts applied as previously used for the three-station analysis.

Figure 5.3 shows the core and angular resolution using only the prototype station as well as the previously presented results for three stations. Comparing both cases the resolutions for the single station is slightly degraded. To quantify this, the best achievable resolutions and the corresponding energies are listed as well. For proton (iron) primaries, the best core resolution is obtained at 13.65 ± 3.50 m (15.26 ± 5.10 m) and an energy of E = 7.3 $\log_{10}(E/\text{GeV})$ (E = 6.6 $\log_{10}(E/\text{GeV})$). The best angular resolution is achieved with 3.03 ± 1.14° (3.21 ± 0.49°) at E = 7.4 $\log_{10}(E/\text{GeV})$ (E = 6.4 $\log_{10}(E/\text{GeV})$).
These values are slightly larger than those obtained for the three-station reconstruction in the previous section 5.5. This clearly demonstrates that better results can already be achieved when three stations are considered instead of only one. The improvement with an increasing number of stations can be attributed to the larger sampling area and the improved geometrical coverage provided by multiple detector positions. As a result, both the shower core and direction can be determined more accurately. This trend indicates that a denser or larger array will further enhance reconstruction performance, particularly at higher primary energies.

---

[1] The reconstruction was performed independently of this work by Dr. Shefali, who kindly provided the reconstructed data.

The presented analysis demonstrates that for showers landing close to the chosen scintillators, a valuable shower reconstruction is obtained. Comparing different reference areas shows that the reconstruction strongly depends on the distance between the shower core and the detector array. The best resolutions can be achieved using a compact area around the stations on the one hand and using multiple stations on the other hand.

Consequently, expanding the array or increasing the station density will further enhance the achievable resolutions, particularly for high-energy events. Even more improvements are expected when the scintillator information is combined with IT data, allowing a more precise reconstruction of both shower core and direction.

6

Muon Propagation

Another part of the analysis is devoted to the IceCube Upgrade. As already explained in Chapter 3.2, the Upgrade includes seven new strings located nearby DeepCore. In this work, the propagation of secondary muons to the Upgrade is investigated in particular, with the aim of gaining insight into how many air showers can actually be detected by the Upgrade. The idea is here to investigate if with Upgrade and scintillators a better measurement of the high-energy muons in the shower core is possible, in particular for low-energy showers. This could be used for more stringent tests on the hadronic interaction models in use at the simulations. This analysis is carried out from two perspectives: on the one hand, considering the results of the muon propagation for the entire simulation dataset, and on the other hand, in relation to the scintillator stations discussed in Chapters 4 and 5.

In both cases, the propagation of muons to the Upgrade volume is considered, as defined in Figure 6.1. The Upgrade strings have the numbers 87 to 93. All DOMs are shown, although the upper ones mainly serve calibration purposes and are not included in the Upgrade volume in the following analysis. The DOMs located at depths of about 2150 m to 2425 m below the surface (in Figure 6.1, where an offset of 1948.07 m is applied, corresponding to roughly -215 m to -480 m) fall in the region, at which the glacial ice is the clearest [27], making them well suited for data acquisition. Thus, these DOMs are taken into account in the analysis. Consequently, the Upgrade volume is defined as the volume enclosing these relevant DOMs and includes a total volume of 736603.21 m^3, which corresponds to 0.07% of the total IceCube volume approximated as 1 km^3.

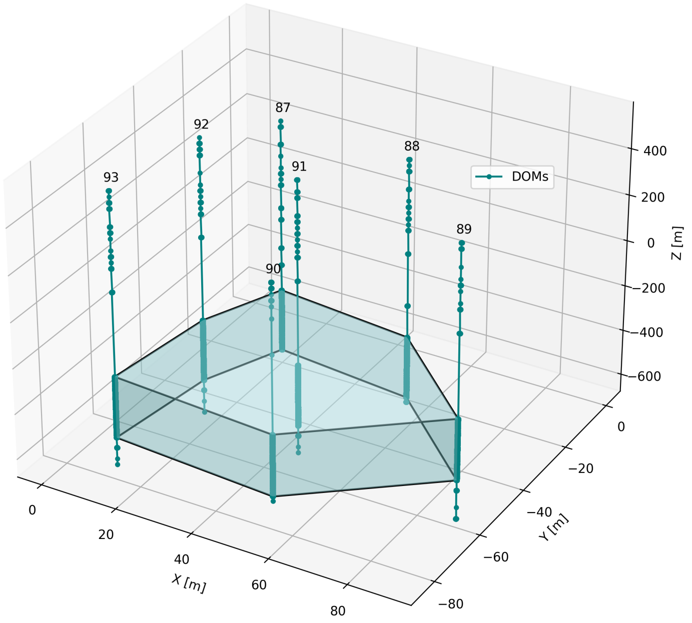

Figure 6.1: Upgrade volume used for the muon propagation. The Upgrade strings 87 to 93 with the individual DOMs can be seen. The DOMs used for data acquisition are contained within the volume shown. The plot includes an offset, where the surface is defined at 1948.07 m.

In the muon propagation, all the muons available from the CORSIKA simulation starting at the surface are tracked through the medium while taking into account all relevant interactions. This is done using the Monte Carlo code PRopagator with Optimal Precision and Optimized

Speed for All Leptons (PROPOSAL) [37]. PROPOSAL calculates the propagation of charged leptons in order to numerically simulate energy losses and scattering processes with high precision. It includes energy losses due to processes such as ionization, bremsstrahlung, photo nuclear interactions, and pair production, as well as particle decay. The calculation itself involves the evaluation of cross section integrals and tracking integrals using advanced numerical methods [37]. This means that after each interaction, information about the remaining energy of the muon is available. It can occur that a muon loses all of its energy before reaching the instrumented detector volume.

Since the Upgrade volume is very small compared to the entire IceCube volume, a large fraction of muons will also never reach it simply due to their initial direction. For this reason, a distinction must first be made between muons that cannot reach the volume because of their direction and those for which it is theoretically possible. The muons that have an energy above a certain threshold and could theoretically reach the volume due to their angle of incidence are defined as *true muons*, with their number denoted as $N_{\mu,\text{true}}$. Studying the further propagation only makes sense for these muons. The subset of muons that actually reach the Upgrade volume are referred to as *observed muons*, and their number is denoted as $N_{\mu,\text{obs}}$.

With these key quantities defined, the following two sections 6.1 and 6.2 present the results of the muon propagation.

6.1 Results Regarding the Entire Dataset

First, the statistics for the entire dataset with primary energies from 10^{12} to 10^{17} eV and zenith angles of 0° to 50° are examined. The use of the entire dataset means that all simulated showers are included, which are distributed across the whole IT array. The results for the full dataset are summarized in Table 6.1, where they are presented both in terms of muon counts (first and second column) and in terms of showers (third and fourth column). In the shower-wise representation, $N_{s,\text{top}}$ denotes the number of showers with cores located within a circle of radius 600 m around the center of the IT array, and $N_{s,\text{vol}}$ indicates how many of these showers contain at least one muon that reaches the Upgrade volume.

primary	$N_{\mu,true}$	$N_{\mu,obs}$	$N_{s,\text{top}}$	$N_{s,\text{vol}}$
H	2682	1152	88625	57
Fe	3072	1247	88932	56

Table 6.1.: Results of the muon propagation regarding the entire dataset as described in appendix A. The dataset has an energy slope of E^{-1} and all the simulations were used. The numbers mentioned in the text are depicted for both primary types proton and iron.

The proton showers (iron showers) contain in total 2682 (3072) true muons, i.e. muons for which the line defined by their starting point and direction would theoretically intersect the Upgrade volume and where the energy is above a threshold of 596.9 ± 5.1 GeV. The determination of this threshold value will be explained in more detail later. However, fewer than half of them, namely 1152 (1247) muons corresponding to 43.0% (40.6%), actually reach the volume. The reduction in the number of muons is caused by energy losses during their propagation through the ice, as described by the interaction processes implemented in PROPOSAL mentioned earlier.

In total, 88625 (88932) proton (iron) showers fall into the specified circular area, but only about 57 (56) showers actually reach the Upgrade volume. A visualization of their core positions and zenith distributions is shown in Figure 6.2. Compared to the total number of showers $N_{s,\mathrm{top}}$, this fraction is very small, corresponding to about 0.064% (0.063%). It should be noted that no cut on the primary energy has been applied for $N_{s,\mathrm{top}}$. Thus, low-energy showers that hardly produce high-energy muons are also included, which naturally leads to a small percentage of showers reaching the volume. Nevertheless, the absolute number of showers inside the volume $N_{s,\mathrm{vol}}$ is also very low. Therefore, a comprehensive and extended analysis of surface-in-ice correlations is not meaningful.

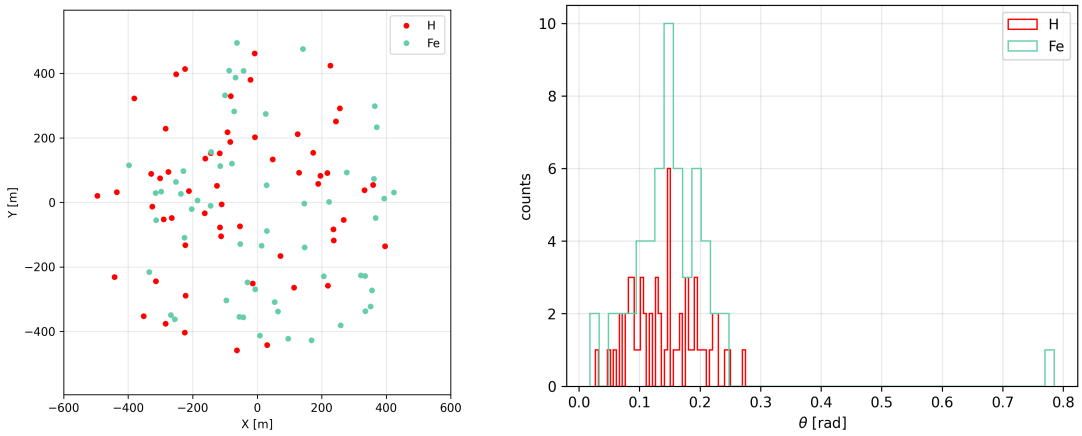

(a)

(b)

Figure 6.2.: Properties of showers reaching the Upgrade volume. Plot (a) shows the core position, while plot (b) shows the corresponding zenith values.

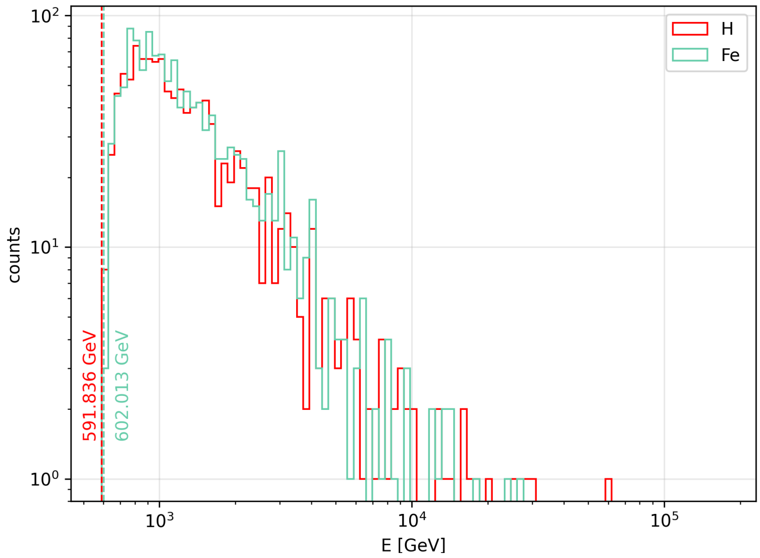

Figure 6.3.: Energy threshold for muons to reach the Upgrade volume. The histogram shows the initial energy of those muons, that actually reach the volume.

Furthermore, the analysis can be refined by examining the energy of the observed muons. Plotting the initial energy of those muons that reach the Upgrade volume allows an estimate of the corresponding energy threshold. As shown in Figure 6.3, the obtained values are 591.8

GeV and 602.0 GeV, with their difference likely attributable to the limited statistics. Hence, muons require a minimum energy of 596.9 ± 5.1 GeV to reach the Upgrade volume. This threshold is already included in the definition of $N_{\mu,\text{true}}$. Additional distributions related to the muon propagation, such as the deposited energy, can be found in appendix D.

6.2 Coincidence Between Scintillator and Upgrade Events

To establish a connection with the previous chapters 4 and 5, which focused on scintillator stations 16, 21, and 25, the results of the muon propagation are also presented for events which are triggered and reconstructed by these stations. Table 6.2 summarizes the number of showers N_s that satisfy different conditions.

	inside sampling area	+ θ<25.84°	+ fulfill min. hits (condition in brackets)	+ at least one true muon	+ at least one observed muon
N_s for H	8696	2827	(3) 1771 (5) 1490 (8) 1205	(3) 10 (5) 10 (8) 8	(3) 9 (5) 9 (8) 8
N_s for Fe	8754	2779	(3) 1547 (5) 1335 (8) 1083	(3) 9 (5) 8 (8) 7	(3) 7 (5) 7 (8) 7

Table 6.2.: Results of the muon propagation regarding the three scintillator stations. The numbers of showers N_s for different conditions are depicted for both primary types proton and iron. Each condition is also explained more in detail in the text.

It becomes evident that the number of showers decreases rapidly once more restrictive conditions are applied. While several thousand showers fall within the sampling area and pass the zenith angle cut, only a small fraction fulfills the additional condition of producing enough hits in the scintillators. The number of events is reduced even further when considering only those showers with at least one true muon that could, in principle, reach the Upgrade volume. Finally, the number of observed muons, i.e. those actually entering the volume, is in the order of only a few events.

This demonstrates that the combination of geometrical constraints and energy losses during propagation strongly suppresses the number of detectable muons. When considering the restriction of the area for showers to land to less than 6% of the total surface array, it becomes clear that this greatly limits the number of showers that could contribute to the volume. The combination of limited scope in the incident angle and the small size of the Upgrade volume compared to the total volume therefore leads to low statistics, which are further reduced by the exclusion of low-energy events due to the energy threshold for muons. It should also be noted that the simulation dataset was primarily designed for the scintillator studies rather than for detailed muon propagation analyses, which may further contribute to the low event statistics observed here.

Consequently, a comprehensive coincidence analysis between surface stations and the Upgrade volume is not feasible.

Although the number of observed events located in the sampling area of the scintillator stations and containing at least one muon in the Upgrade volume is very small, it is still instructive to examine how well these events can be reconstructed.

The focus is on showers with at least three scintillator hits, corresponding to nine proton

	x [m]	y [m]	z [m]	θ [rad]	ϕ [rad]	E [GeV]	N_{obs}	$\hat{E}_\mu$ [GeV]	Δr [m]	α [°]
H	-84.24	187.68	1958.08	0.13	4.13	1.46×10^5	1	865.28	86.86	2.68
	-116.16	152.13	1958.08	0.12	4.33	6.62×10^5	4	968.1 ± 93.28	10.58	0.92
	-125.24	51.23	1958.08	0.10	4.68	2.82×10^6	10	2394.3 ± 931.82	3.77	0.98
	-161.14	135.70	1958.08	0.15	4.49	5.81×10^6	1	1265.93	8.26	1.35
	-92.14	217.29	1958.08	0.15	4.21	2.38×10^7	31	1464.2 ± 132.51	2.05	4.08
	-143.85	152.99	1958.08	0.11	4.40	5.91×10^7	14	1138.4 ± 262.62	13.35	1.09
	-110.59	-6.09	1958.08	0.07	4.74	5.95×10^7	183	1704.1 ± 97.39	37.32	2.74
	-211.75	35.17	1958.08	0.13	5.02	8.62×10^7	4	909.3 ± 200.02	13.99	2.18
	-162.89	-33.17	1958.08	0.09	4.94	8.59×10^7	7	991.9 ± 142.65	35.77	3.05
Fe	-185.44	5.83	1958.08	0.13	4.97	4.98×10^5	1	991.16	13.45	3.02
	-144.85	-10.66	1958.08	0.09	4.94	6.31×10^5	5	1700.7 ± 614.27	22.59	9.48
	-143.56	156.52	1958.08	0.14	4.45	1.03×10^6	8	1563.5 ± 288.50	40.91	1.92
	-203.63	-20.55	1958.08	0.11	5.00	8.45×10^6	54	1965.3 ± 352.16	16.73	2.85
	-114.74	112.83	1958.08	0.12	4.58	2.74×10^7	3	955.9 ± 96.18	10.21	1.00
	-236.64	27.00	1958.08	0.15	5.04	2.95×10^7	2	801.9 ± 170.53	8.01	4.03
	-78.99	120.74	1958.08	0.08	4.22	4.30×10^7	5	1046.2 ± 116.89	10.17	3.27

Table 6.3.: Coincidence between scintillator and Upgrade events. For those showers, that fall into the sampling area with $\theta \lesssim 26°$, trigger at least 3 scintillator panel pairs, and have at least one muon reaching the Upgrade volume, the primary position, direction and energy is shown, as well as the number of muons in the Upgrade volume and their mean initial energy. The last two columns show the core and angular accuracy for the reconstruction of those events, i.e. the distance between the reconstructed and true primary core positions, and the space angle between the reconstructed and true directions.

and seven iron events. For each of these, Table 6.3 lists the core position, shower direction, primary energy, the number of muons in the Upgrade volume, and their mean energy. As reconstruction indicators, the core accuracy (distance between true and reconstructed core) and angular accuracy (space angle between true and reconstructed direction) are given. While some events are reconstructed with deviations of only a few meters, others show larger discrepancies. Similarly, the angular accuracy varies across the sample. However, due to the very limited statistics, no general or robust conclusions can be drawn. Table 6.3 is therefore mainly intended to illustrate the coincidence between scintillator and in-ice events.

Overall, the limited statistics of the simulation set do not allow for a conclusive statement, neither for the entire dataset nor for the analysis of the events in connection with the scintillators. However, it could be shown that events that combine information from the scintillator stations and the Upgrade do exist and can be detected and analyzed after an appropriate measurement time.

7

Summary and Outlook

The IceCube experiment is currently being enhanced with several new components. Two of these upgrades are a surface array of 32 scintillator stations, each equipped with eight panels, and the in-ice IceCube Upgrade. The latter consists of seven new strings, whose smaller spacing significantly lowers the energy threshold for neutrinos. This opens new opportunities for the study of neutrino oscillations. At the same time, both the scintillators and the IceCube Upgrade can be employed for the investigation of EASs, with the aim of gaining further insights into CR studies.

Since these upgrades are close to installation, simulation studies represent a crucial tool to make predictions about the performance of the new detector systems in advance. Within this framework, detector responses are generated and subsequently analyzed with respect to efficiency and reconstruction accuracy. This constitutes the subject of the present thesis.

In the first part, three scintillator stations recently deployed and brought into operation were investigated with regard to their efficiency in detecting air showers as well as their core and angular resolution when reconstructions are based solely on these three stations.
To ensure representative results, the sampling area was specifically adapted to the geometry of these stations. For this area, the detection efficiency of the scintillators could then be determined. Under the trigger condition of at least three hits distributed across the three stations, the 90% efficiency for proton primaries is reached at an energy of 1.74×10^5 GeV. For iron primaries, the corresponding value is 2.63×10^5 GeV.
The obtained efficiency values can be considered very reasonable for the given three-station setup. It indicates that the detectors perform well within the intended energy range. It should be noted, however, that the absolute values depend strongly on the chosen sampling area and trigger definition. The larger the area considered, the higher the energy at which the 90% efficiency is achieved. But for the final chosen sampling area, the results are encouraging and give a basis for future analyses using similar conditions.

Reconstruction resolutions were also evaluated. These values quantify how precisely properties of the primary particle can be reconstructed, here focusing on the core position and arrival direction. The best results are obtained when only events in the area of the three stations are considered. For the same sampling area used in the efficiency study, the best core resolution was achieved at 7.94×10^6 GeV with 6.08 ± 3.40 m for proton generated showers and 6.23 ± 1.41 m for iron generated showers. The best angular resolution occurred at 2.00×10^6 GeV with $2.09 \pm 0.44^\circ$ for proton showers and $2.05 \pm 0.76^\circ$ for iron showers.
The obtained reconstruction resolutions demonstrate a solid performance of the detectors, especially considering that only three stations were used for the reconstruction without any information from IT. For events with cores located close to the scintillators, both the core and angular resolutions reach meaningful values for the shower reconstruction.

In the second part of the thesis, muon propagation to the IceCube Upgrade was studied. For this purpose, a volume around the new strings was defined, and showers were analyzed to determine whether their muons reached this volume. The analysis yielded a muon energy threshold of 596.9 ± 5.1 GeV. Among all showers with cores landing within a radius of 600 m from the center of the surface array, 57 proton showers and 56 iron showers (corresponding to around 0.06% of all showers each in the energy range 10^{12} to 10^{17} eV with energy slope E^{-1}) were found to produce muons in the Upgrade volume.
When restricting the sample to showers that additionally satisfy the previously defined trigger condition, only 9 proton and 7 iron showers remained. Due to this limited statistics, no detailed surface–in-ice correlation could be studied. However, as data provides much more statistics than can be simulated, there will be events where the Upgrade measurements can be used.

The efficiency results are encouraging, as they indicate that air showers can be reliably detected already at lower energies. It should be emphasized that this analysis was restricted to only three stations, whereas the full array will consist of 32 stations. This is expected to further increase the efficiency and thus improve the measurement of EASs. In combination with other detector components, such as the existing Cherenkov tanks or radio antennas, a significant enhancement of performance can be anticipated.
The comparison of the resolutions based on three vs. one scintillator station also demonstrates that even three stations already provide an improvement over reconstructions based on a single station. With a complete scintillator array, further progress in directional and core reconstruction is expected. An analysis that includes all scintillator stations therefore represents a possible next investigation, but is beyond the scope of this thesis. Also combining data from IT and the scintillators will improve the accuracy in reconstruction of the EAS.
With respect to muon propagation, it should be noted that the small number of events is partly due to the limited size of the defined Upgrade volume relative to the overall detector. In addition, the simulation dataset used was originally generated for scintillator studies and not specifically for muon analyses. Consequently, an investigation based on dedicated simulations might yield different or more robust results. In particular, a comprehensive surface–in-ice correlation analysis could provide valuable insights into the performance of combining the detector systems.

Bibliography

---

[1] P. Biermann et al. *Introduction to Cosmic Rays*. 2002. URL: `https://doi.org/10.48550/arXiv.astro-ph/0202425`.

[2] A. Leszczynska. *Potential of the IceTop Enhancement with a Scintillation Detector Array*. Doctoral Thesis in Physics at Karlsruhe Institute Of Technology (KIT). Karlsruhe, 2020.

[3] M. Tanabashi et al. *Review of Particle Physics*. Particle Data Group. 2018. URL: `https://doi.org/10.1103/PhysRevD.98.030001`.

[4] IceCube Collaboration. *IceCube Neutrino Observatory*. URL: `https://icecube.wisc.edu` (visited on 04/25/2025).

[5] T. Waldenmaier. *IceTop — Cosmic ray physics with IceCube*. IceCube Collaboration. 2008. URL: `https://doi.org/10.1016/j.nima.2008.01.015`.

[6] K. Hanson et al. *Scope Management Plan for the IceCube Upgrade Project*. 2022. URL: `https://docushare.icecube.wisc.edu/dsweb/Get/Rendition-138641/unknown`.

[7] V. F. Hess. *Über Beobachtungen der durchdringenden Strahlung bei sieben Freiballonfahrten*. Physik. Zeitschrift XIII. 1912.

[8] F. Riggi. *Messengers from the Cosmos. An Introduction to the Physics of Cosmic Rays in Its Historical Evolution*. Springer, 2023. URL: `https://doi.org/10.1007/978-3-031-24762-0`.

[9] J. Matthews. *A Heitler model of extensive air showers*. 2004. URL: `https://doi.org/10.1016/j.astropartphys.2004.09.003`.

[10] L. Cazon. *Extensive Air Showers: from the muonic smoking guns to the hadronic backbone*. 2021. URL: `https://doi.org/10.48550/arXiv.1301.3340`.

[11] A. Watson. *The discovery of Cherenkov radiation and its use in the detection of extensive air showers*. 2011. URL: `https://doi.org/10.48550/arXiv.1101.4535`.

[12] S. Navas et al. *34. Passage of Particles Through Matter*. Review of Particle Data Group. 2024.

[13] M. G. Aartsen et al. *The IceCube Neutrino Observatory: instrumentation and online systems*. Publishing for Sissa Medialab. 2017. URL: `https://iopscience.iop.org/article/10.1088/1748-0221/12/03/P03012`.

[14] F. Varsi. *Measurement of the energy spectrum and composition of cosmic rays by the GRAPES-3 experiment*. Doctoral Thesis in Physics at Indian Institute of Technology Kanpur. 2023.

[15] J. A. Aguilar. *Highlights from the IceCube Neutrino Observatory*. IceCube Collaboration. 2025. URL: `https://doi.org/10.1051/epjconf/202531902003`.

[16] P. Koundal. *Elemental Composition Of Cosmic Rays. Analysis Of IceCube Data Using Graph Neural Networks*. Doctoral Thesis in Physics at Karlsruhe Institute of Technology (KIT). Karlsruhe, 2023.

[17] V. Verzi. *Measurement of the energy spectrum of ultra-high energy cosmic rays using the Pierre Auger Observatory*. Pierre Auger Collaboration. 2019. URL: `https://doi.org/10.22323/1.358.0450`.

[18] M. G. Aartsen et al. *IceCube-Gen2: A Vision for the Future of Neutrino Astronomy in Antarctica*. IceCube Collaboration. 2014. URL: `https://doi.org/10.48550/arXiv.1412.5106`.

[19] A. Haungs. *A Scintillator and Radio Enhancement of the IceCube Surface Detector Array*. IceCube Collaboration. 2019. URL: `https://doi.org/10.1051/epjconf/201921006009`.

[20] M. Weyrauch. *Simulation Study for the IceCube-Gen2 Surface Array*. Master's Thesis in Physics at Karlsruhe Institute Of Technology (KIT). Karlsruhe, 2021.

[21] M. Plum et al. *Simulation and Reconstruction Study of a Future Surface Scintillator Array at the IceCube Neutrino Observatory*. IceCube Collaboration. 2019. URL: `https://doi.org/10.48550/arXiv.1909.02258`.

[22] W. R. Leo. *Techniques for Nuclear and Particle Physics Experiments*. Springer Nature Link, 1994. URL: `https://doi.org/10.1007/978-3-642-57920-2_7`.

[23] G. F. Knoll. *Radiation detection and measurement - 4th edition*. John Wiley & Sons, Inc., 2010.

[24] T. Huber et al. *The IceTop Scintillator Upgrade*. IceCube-Gen2 Collaboration. 2017. URL: `https://doi.org/10.22323/1.301.0401`.

[25] M. Kauer et al. *The Scintillator Upgrade of IceTop: Performance of the Prototype Array*. IceCube Collaboration. 2019. URL: `https://pos.sissa.it/358/309`.

[26] Wikipedia. *Silicon photomultiplier*. URL: `https://en.wikipedia.org/wiki/Silicon_photomultiplier` (visited on 05/17/2025).

[27] A. Ishihara. *The IceCube Upgrade - Design and Science Goals*. IceCube Collaboration. 2019. URL: `https://doi.org/10.48550/arXiv.1908.09441`.

[28] M. G. Aartsen et al. *IceCube-Gen2: The Window to the Extreme Universe*. IceCube-Gen2 Collaboration. 2020. URL: `https://arxiv.org/abs/2008.04323`.

[29] A. Coleman et al. *Simulation study for the future IceCube-Gen2 surface array*. IceCube-Gen2 Collaboration. 2022. URL: `https://doi.org/10.48550/arXiv.2108.04307`.

[30] D. Heck et al. *CORSIKA: A Monte Carlo code to simulate extensive air showers*. 1998. URL: `https://publikationen.bibliothek.kit.edu/270043064`.

[31] A. Leszczynska et al. *A multi-detector EAS reconstruction framework for IceCube*. IceCube Collaboration. 2023. URL: `https://doi.org/10.22323/1.444.0366`.

[32] C. Dormann. *Parametrische Statistik. Verteilungen, maximum likelihood und GLM in R*. Springer Spektrum, 2013. URL: `https://doi.org/10.1007/978-3-642-34786-3`.

[33] K. Kamata and J. Nishimura. *The Lateral and the Angular Structure Functions of Electron Showers*. 1958. URL: `https://doi.org/10.1143/PTPS.6.93`.

[34] H. Abramowicz et al. *Measurement of shower development and its Molière radius with a four-plane LumiCal test set-up*. in The European Physical Journal C. 2018. URL: `https://doi.org/10.1140/epjc/s10052-018-5611-9`.

[35] Studyflix. *Perzentil*. URL: `https://studyflix.de/statistik/perzentil-2041` (visited on 09/17/2025).

[36] V. Justus et al. *Bootstrap confidence intervals: A comparative simulation study*. 2024. URL: `https://doi.org/10.48550/arXiv.2404.12967`.

[37] J.-H. Koehne et al. *PROPOSAL: A tool for propagation of charged leptons*. in Computer Physics Communications. 2013. URL: `https://doi.org/10.1016/j.cpc.2013.04.001`.

List of Abbreviations

AMANDA	Antarctic Muon and Neutrino Detector Array
CORSIKA	COsmic Ray SImulations for KAscade
CR	Cosmic Ray
DAQ	Data Acquisition
D-Egg	Dual optical sensors in an Ellipsoid Glass for Gen2
DLP	Double Logarithmic Paraboloid
DOM	Digital Optical Module
EAS	Extensive Air Shower
ICNO	IceCube Neutrino Observatory
IT	IceTop
LDF	Lateral Distribution Function
MIP	Minimum Ionizing Particle
mDOM	Multi-PMT Digital Optical Module
NKG	Nishimura, Kamata and Greisen
PMT	Photo Multiplier Tube
PROPOSAL	PRopagator with Optimal Precision and Optimized Speed for All Leptons
SFH	Scintillator Field Hub
SiPM	Silicon Photo Multiplier
SPAD	Single-Photon Avalanche Diode
VEM	Vertical Equivalent Muon

A

Simulation Dataset

The following Table A.1 gives an overview on the key parameters of the simulated dataset. It was created by Agnieszka Leszczynska for her doctoral thesis in [2]. Originally, there are five primary types. In this thesis, only proton (H) and iron (Fe) are used. The energy distribution of these primaries can be seen in Figure A.1.

parameter	**set value**
particle types	H, Fe
primary energy range	$10^{12} – 10^{17}$ eV
zenith angle range	0° – 50°
azimuth angle range	-180° – 180°
particle energy cut	20 MeV, 100 keV
energy slope	-1 (within every energy decade)
hadronic interaction model below 80 GeV	FLUKA
hadronic interaction model high energy interactions	SIBYLL 2.3c

Table A.1.: Parameters of the simulation dataset used for the analysis.

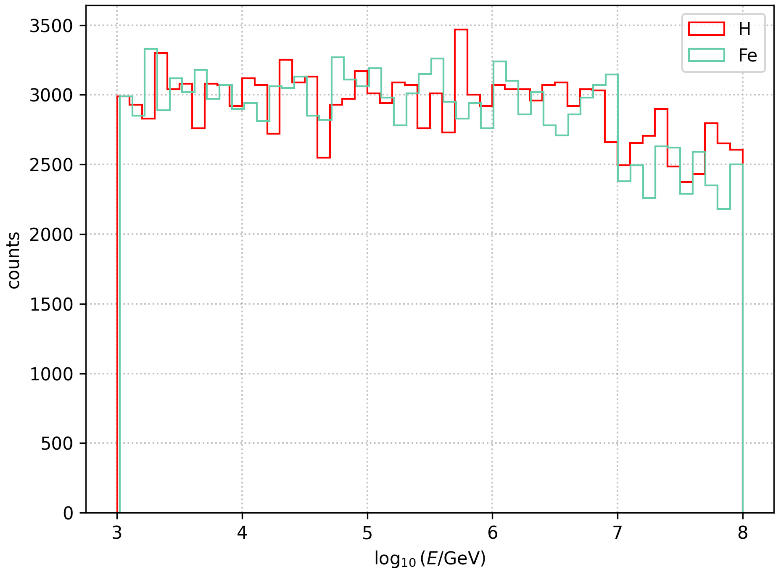

Figure A.1.: Energy distribution of the dataset for the primary types proton and iron.

B

Efficiency for Rectangular Sampling Areas

During the development of the final sampling area, the efficiency was also calculated for enlarged and reduced rectangular areas. These can be seen in Figure B.1.

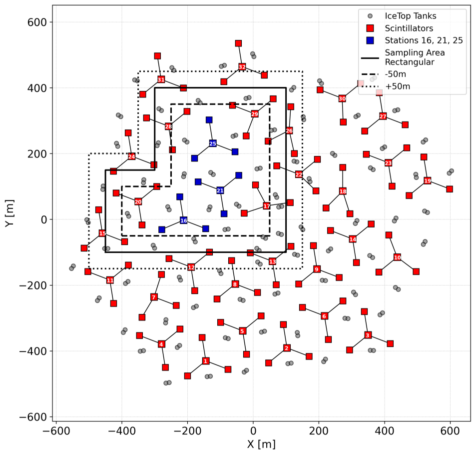

Figure B.1: Rectangular sampling areas. The rectangular sampling area used in this thesis is depicted here, including a reduction and extension of 50 m.

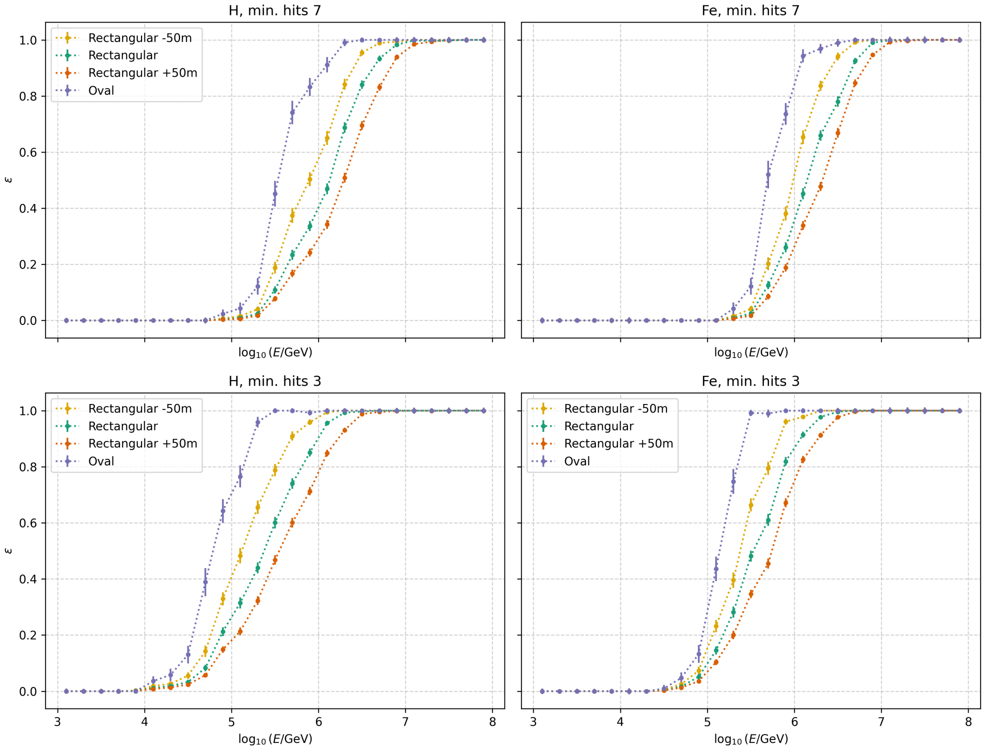

Figure B.2.: Efficiency for rectangular areas. It was calculated for both proton and iron with at least 3 or 7 minimum hits. The different curves correspond to different sampling areas. For comparison, the curve for the final oval sampling area is also shown.

C

Distributions in the Resolution Analysis

The underlying distributions used for the calculation of the 68-percentile for the resolutions are shown below. If there are less than 10 counts in one distribution, it was not taken into account.

C.1 Δr Distributions

Figure C.1.: Δr distributions for iron. The curves represent different conditions for the showers used in the respective resolution in chapter 5.4.

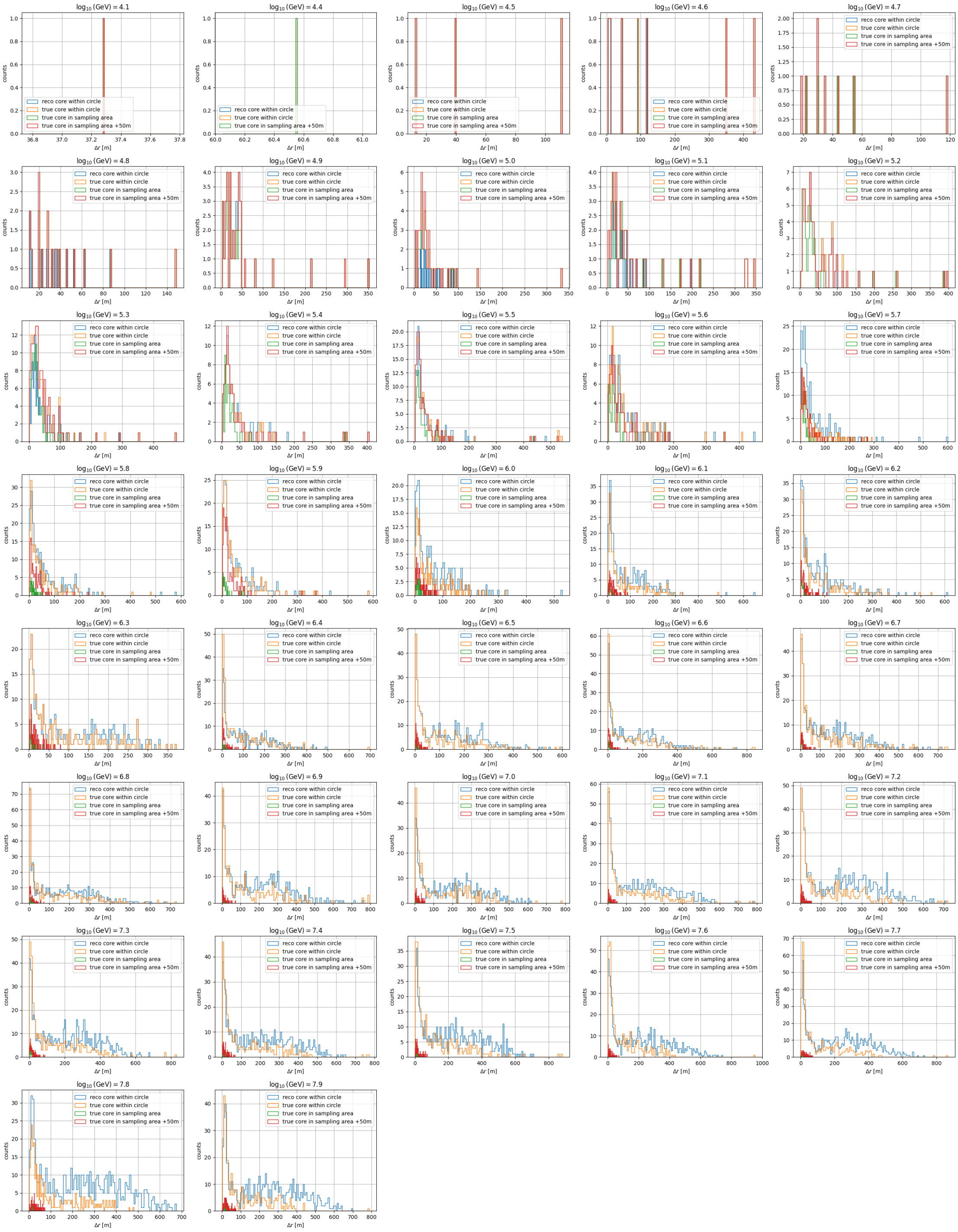

Figure C.2.: Δr distributions for proton. The curves represent different conditions for the showers used in the respective resolution in chapter 5.4.

C.2 Space Angle Distributions

Figure C.3.: α distributions for iron. The curves represent different conditions for the showers used in the respective resolution in chapter 5.4.

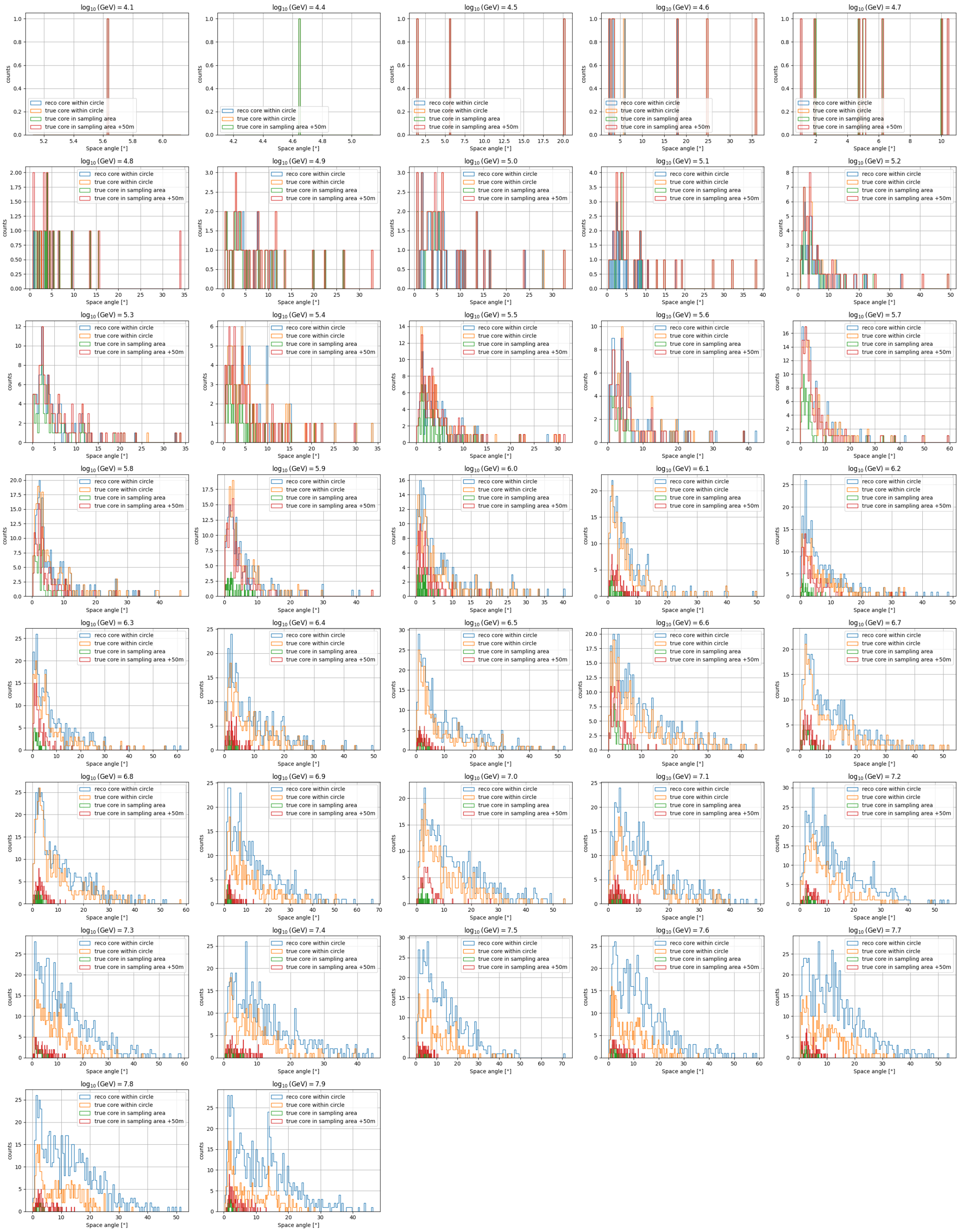

Figure C.4.: α distributions for proton. The curves represent different conditions for the showers used in the respective resolution in chapter 5.4.

D Muon Propagation Distributions

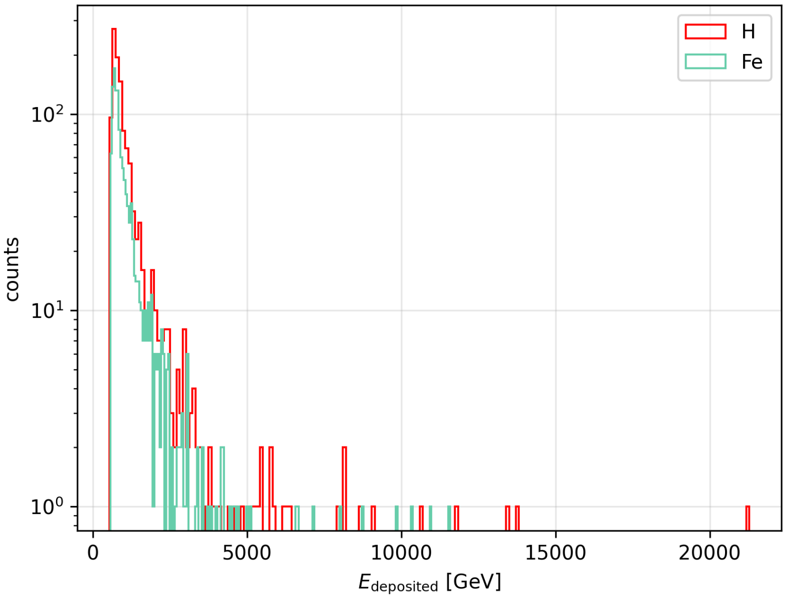

Figure D.1.: Approximation of the energy deposit of the muons that are propagated to the Upgrade volume.

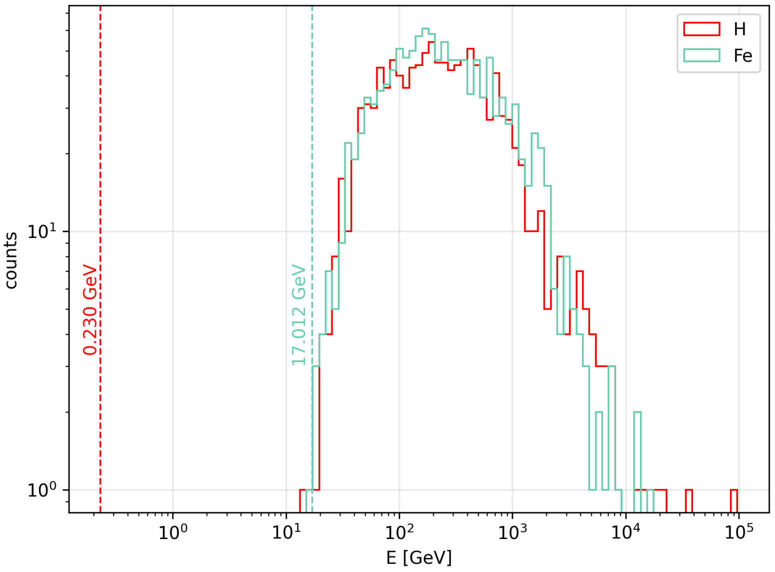

Figure D.2.: Energy distribution of the muons at the time of entering the Upgrade volume. For those muons, that reach the Upgrade, the energy right before entering the volume is plotted. The minimum value is additionally marked with a vertical line.

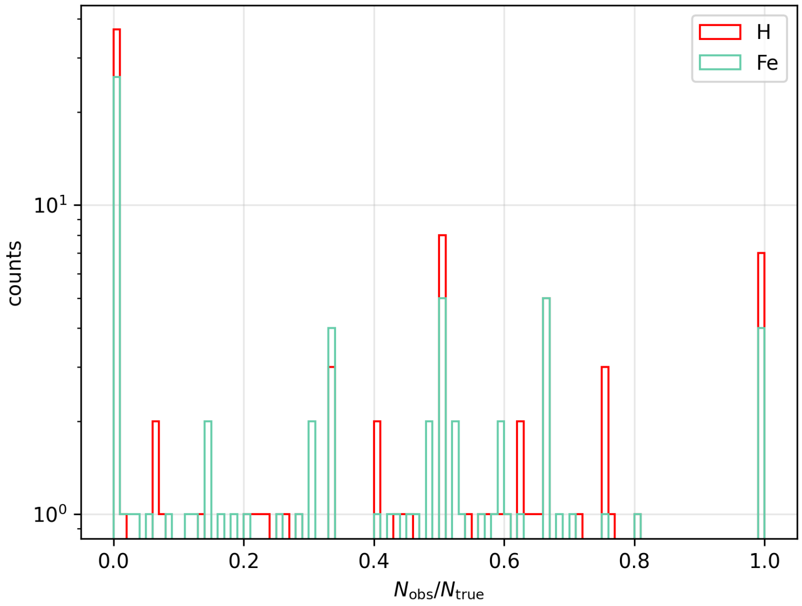

Figure D.3.: Ratio of true and observed muons. For each event, the number of observed muons divided by the number of true muons is plotted.

Acknowledgements

Without the support of many people, this thesis could not have taken its final form. I would therefore like to express my gratitude to all those who contributed.

My sincere thanks go to Prof. Dr. Ralph Engel and Dr. Andreas Haungs, who served respectively as supervisor and examiner of this work. I am especially grateful for the guidance of Prof. Dr. Ralph Engel, whose advice gave the thesis its structure and clarity. I also greatly appreciate the constructive feedback and valuable input from Dr. Andreas Haungs, which consistently helped to improve the content. His kindness and warm demeanor created an atmosphere in which I always felt genuinely welcome.

My deepest gratitude goes to Dr. Fahim Varsi, who advised me throughout every step of this journey. His detailed theoretical explanations introduced me to cosmic ray physics and the IceCube experiment in a way that was both thorough and inspiring. I could always turn to him with questions and received helpful answers. No matter the circumstances, whether on weekends or during holidays, he was a patient, reliable, and friendly mentor. Thank you for your teaching and guidance.

I would also like to thank all members of the IceCube group at KIT. Through our fruitful discussions, both during and outside of the Friday meetings, I received valuable suggestions and new ideas. In particular, I am grateful to Dr. Shefali, Mark Weyrauch, and Dr. Federico Bontempo for providing useful scripts, which I could adapt to my own work, as well as for their openness in answering my questions and introducing me further to IceCube.
Many thanks as well to Sabine Bucher for her administrative support and to Doris Wochele for introducing me to the world of computing.

Together, all of these people have accompanied me throughout the process and helped shape this thesis into its best possible form. I will look back on this time with gratitude and carry the knowledge and experience I have gained into my future academic path.